A Study of Miniature Methods of Terahertz Spectroscopy

by

Andrew Nicholas Hone
B.Eng., University of Victoria, 2006

A Thesis Submitted in Partial Fulfillment of the
Requirements for the Degree of

Master of Applied Science

in the Department of Electrical and Computer Engineering

A Study of Miniature Methods of Terahertz Spectroscopy

by

Andrew Nicholas Hone
B.Eng., University of Victoria, 2006

Supervisory Committee

Dr. Thomas E. Darcie, Supervisor
(Department of Electrical and Computer Engineering)

Dr. Jens Bornemann, Departmental Member
(Department of Electrical and Computer Engineering)

Supervisory Committee

Dr. Thomas E. Darcie, Supervisor
(Department of Electrical and Computer Engineering)

Dr. Jens Bornemann, Departmental Member
(Department of Electrical and Computer Engineering)

ABSTRACT

Compared to the history of science, spectroscopy at terahertz frequencies is a relatively recent development. Terahertz instruments were initially large and inefficient due to the characteristics of available technology. With progress in materials science and miniature circuit manufacturing techniques, we may fabricate micro-meter scale devices to generate and detect terahertz radiation. However, the complete spectroscope apparatus remains large due to the use of components such as lenses and mirrors designed in the far-field optical regime. A truly miniature terahertz spectroscope would be designed without lenses and mirrors to enable a wide range of inexpensive and pervasive applications in diverse fields such as medicine, materials identification, and security. We present detailed evaluation of some candidate structures for a quasi-optical device and design criteria for a quasi-TEM transmission-line based device. Quasi-TEM transmission lines are inherently broadband and therefore suited for use in a spectroscope.

Contents

List of Tables

List of Figures

ACKNOWLEDGEMENTS

I would like to thank:

Dr. T. E. Darcie, for mentoring, support, encouragement, and patience.

Dr. J. Bornemann, for use of computing resources and valuable discussions on computational electromagnetics.

DEDICATION

Dedicated to the memory of my grandmother, B. V. (Tappy) Hone.

Part I

Introduction and related work

Chapter 1

Introduction

Science using electromagnetic waves at terahertz frequencies is a relatively new but fertile and intriguing field. Terahertz waves are between the limits of many practical electronic and optical technologies but can be applied in interesting ways. For example, terahertz waves can reveal details of chemical structure of plastics or stars, or pass through some materials to image their contents. Because terahertz waves do not ionize matter like X-rays, terahertz measurement systems can be non-destructive and generally safe for operators and subjects. Because the size of an apparatus using electromagnetic waves is approximately related to the working wavelength, terahertz devices could be compact, at scales of tens to hundreds of micrometers. Terahertz devices are often not made compact due to efficiency gains in using large geometric optics apparatus. An example of such an apparatus in a laboratory setting is provided in Figure 1.1. In this work, we investigate and propose design criteria for a terahertz spectroscope using tightly confined near fields, enabling construction of a compact device.

While there is no strict definition of the range of frequencies which bound the terahertz range, we can place arbitrary bounds based on the qualitative difficulty of performing science between approximately 300 GHz to 3 THz. In low-energy physics there are generally two methods of generating electromagnetic waves: movement of charge, and stimulated emission of an atomic or molecular system. Traditional semiconductor sources such as transistors may not be able to generate useful power above frequencies of several hundred gigahertz. Traditional photonic sources, such as lasers based on population inversion between atomic or molecular energy levels, may not be able to generate useful and frequency tunable power below several tens of terahertz. Our objective of a miniature terahertz spectroscope places some restrictions

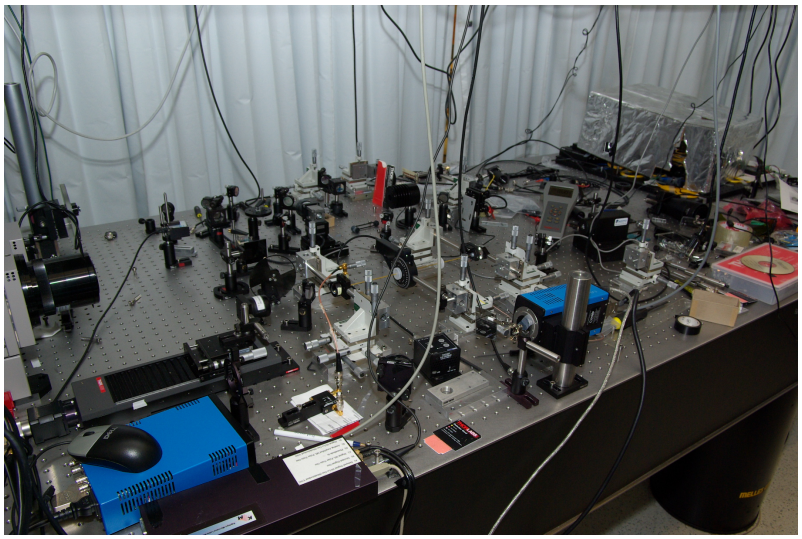

Figure 1.1: An example of an optical table for several terahertz experiments with sufficient space for geometric optics.

on the physical size of the source and detector. We review some methods to generate and detect electromagnetic waves in the terahertz gap in Sections 2.1 and 2.2.

The small scale of terahertz systems has required ingenuity in designing structures which may be practically fabricated. Many terahertz devices are familiar analogs of RF or optical frequency devices modified for planar fabrication techniques. We review possible structures for further consideration as a miniature terahertz spectroscope in Section 2.3.

Spectroscopy may be performed in either a transmission or reflection mode. In transmission spectroscopy, the excitation is measured after passing through a sample. In reflection spectroscopy, the excitation is measured after reflecting from the sample. A spectroscopy experiment may be performed in either mode depending on the phenomenon under study and the characteristics of the material. For example, absorption spectroscopy of a strongly reflecting material, such as gold under infrared illumination, is often performed in reflection. Absorption spectroscopy is one of a wide spectrum of methods, but is the primary method of interest in the terahertz range. Since some materials have unique loss characteristics at terahertz frequencies, a spectroscope may allow the user to estimate the composition and amounts of materials in a sample.

The goal of this work is the evaluation of miniature devices for suitability for terahertz spectroscopy. Since we chose to evaluate these devices by numerical simulation,

we also evaluated computational electromagnetic codes for suitability for simulation of terahertz systems. As terahertz systems are often constructed from dispersive materials or transmission lines, computer simulation of these systems is complicated by requirements for dispersive models of materials and special treatment for transmission lines. These material models and simulation techniques are discussed in Part II.

The models and techniques of Part II are used in Part III to evaluate three miniature devices for terahertz spectroscopy. These devices do not form a complete set of devices which could be used for miniature terahertz spectroscopy, but are presented as representatives of planar devices. Planar devices can be fabricated with standard lithographic techniques and are a standard choice.

We conclude in Chapter 8 that the covered transmission line studied and presented in Chapter 6 is suitable for further investigation as a terahertz spectroscope. The covered transmission line device showed a high contrast between lossy and non-lossy samples with a simple configuration and most importantly no terahertz optics. The remaining challenge is a broadband de-embedding procedure for highly dispersive transmission lines.

We summarize our contributions to the field in Chapter 9, including new simulation results of coupled planar antennas, new simulation results of reflection coupled planar waveguides, and verification of radiation loss mechanisms at terahertz frequencies.

Chapter 2

Related work

Interest in the terahertz range of the electromagnetic spectrum is relatively new, as the technologies required to work in the range only became available in the 20th century. Because of the novelty of the field and the practical use of physical effects in the terahertz range, the field is fertile. While some work on miniature terahertz spectroscopes has been previously published [1, 2], that work focuses on far-field pulsed systems. Several comprehensive review papers have been published covering various apparatus and methods of interest in terahertz spectroscopy [3–5]. In this chapter, we briefly review selected topics relevant to following chapters.

2.1 Methods of terahertz generation

As mentioned in the Introduction, generating terahertz waves is beyond the capability of most conventional electrical and optical systems. Many novel technologies have been invented to fill this gap, including an observation that peeling adhesive tape produces terahertz radiation [6]. Clearly, peeling tape is not suitable for a miniature terahertz spectroscope. While a complete treatment of the theory and practice of terahertz generation and detection is beyond the scope of this work, we present a brief review of terahertz sources compatible with planar devices.

The miniature and planar nature of the spectroscopes proposed in Chapter 6 practically eliminates several popular methods for terahertz generation, such as the free electron laser [7]. However, any device which could be attached to a planar substrate and can couple into planar metal structures could be used. We anticipate the terahertz generation method of choice for the proposed terahertz spectroscope

will be photomixing in a semiconductor due to wide tunability, no moving parts, and room temperature operation. A quantum cascade laser could be used if the target spectroscope application can be cooled to cryogenic temperatures. Saeedkia et al. have written a comprehensive treatment of terahertz generation by photomixing [8].

Photoconduction, also known as the internal photoelectric effect, in a semiconductor can be exploited to produce terahertz waves in a pulsed, time-domain system or a continuous-wave, frequency-domain system. There are some similarities between the approaches, such as the requirement for lasers with photon energy exceeding the band gap of the semiconductor. In a pulsed system, the exciting laser generates pulses with an intensity envelope according to the desired terahertz frequency spectrum. This pulse causes transient photoconductivity in the dc biased photoconductor, which causes a transient photocurrent to flow. In a continuous-wave system, two exciting lasers differing in frequency by the desired terahertz output frequency are superimposed inside the semiconductor. The lasers induce photoconductivity in the semiconductor, which is dc biased to allow a time-varying photocurrent to flow. This continuous-wave process is termed photomixing.

2.2 Methods of terahertz detection

Prior to the use of semiconductors, among other techniques, detection of terahertz radiation was limited to steady-state intensity. Some common instruments which were used in the first terahertz experiments are bolometers and Golay cells [9, 10]. Intensity detectors continue to be used today due to superb broadband frequency response and the ability to be cooled to temperatures approaching absolute zero. These intensity detectors were later incorporated into instruments such as the Fourier transform infrared (FTIR) spectrometer capable of simultaneously measuring the index of refraction and extinction coefficient [11].

The development of semiconductor photomixers heralded the age of terahertz time-domain spectroscopy, where the field amplitude of a repeating terahertz pulse is sampled by changing the phase of the laser field incident on the detector. In addition to the advantages of simultaneously measuring the complex propagation of a pulse, semiconductor photomixers can be mere microns in size, enabling new applications for miniature terahertz spectroscopy.

A photomixing detector functions in a different manner than a generator. The incoming terahertz field self-biases the photomixer, generating a current which is

read by an ammeter. Saeedkia et al. also have written a comprehensive treatment of terahertz detection by photomixing [8].

2.3 Classification of terahertz apparatus

Apparatus for terahertz experiments can be classified according to the nature of the field's interaction with its surroundings. Textbooks on antenna theory commonly divide the space surrounding a radiating object into three parts: reactive near-field, radiating near-field, and far-field. These terms represent the validity of mathematical approximations and are not strict divisions. Additionally, some guidelines for determining these distances are qualified by the condition that the largest antenna dimension is sufficiently larger than the operating wavelength [12].

Near-field devices are typically defined by close object spacing and tight coupling between elements. Far-field devices are typically intended to be used many wavelengths from the source, where the propagating wave can be considered to be in free space with no direct coupling to the source. This division of space can be used to divide terahertz devices into near and far-field categories.

2.3.1 Far-field

The analysis of the far-field characteristics of a radiating structure is often easier than the near-field characteristics due to negligible coupling between source and receiver and approximations of the uniformity of the field, such as the plane wave or paraxial approximations. These analytical characteristics, along with the ease of construction and tuning, make the canonical terahertz spectroscopy apparatus popular. Far-field terahertz devices can be further classified into broadside or end-fire devices. When all antenna elements lie in a plane, a broadside antenna emits most radiation perpendicular to the plane while an end-fire antenna emits most radiation parallel to the plane.

Broadside

Broadside antennas are by far the most common type of antenna employed in terahertz systems. They can be seen in many forms, including planar bi-cones, dipoles, spirals, slots, and more. These planar antennas are often mounted on a silicon hyperhemisphere to exploit the tendency of antennas planced on semi-infinite dielectric

substrates to radiate most of their power into the substrate [13–15]. Some combinations of antennas and lenses exhibit very narrow beamwidth, such as approximately six degree half-power beamwidth at 300 GHz from a planar spiral antenna [16]. However, with our stated objective in the Introduction to minimize the size and cost of a terahertz spectroscope, a large, high-purity, precisely machined silicon lens is a natural choice to replace for cost reduction. If we wish to design a planar antenna without a silicon lens, we must attempt to design the antenna to produce similar directivity as a lens-coupled antenna.

Some improvement to antenna directivity can be made with the application of some thickness of dielectric [17] or metamaterial [18] over a planar antenna with a ground plane. While impressive gains can be made in beamwidth and gain, these improvements come at the cost of reduced bandwidth, disqualifying this particular solution for a broadband terahertz spectroscope.

End-fire

End-fire antennas are much less common than broadside antennas for terahertz applications mostly because an antenna on a semi-infinite dielectric substrate tends to radiate into that substrate. Many common antenna designs, such as the Yagi-Uda, are designed to operate in a region of homogeneous dielectric such as free space. Therefore, an end-fire antenna for terahertz applications should either be located on a thin membrane [19] or be fully encased in dielectric to allow the use of standard end-fire designs.

Common end-fire antennas designed for terahertz frequencies are analogs of their microwave counterparts, such as slotline horns, Yagi-Uda antennas [19], and TEM horns [20, 21]. A TEM horn antenna is defined by a transverse field distribution at the antenna aperture. One way to accomplish this is by constructing an antenna with two or more separate conductors. A common characteristic of terahertz end-fire antenna designs is the care taken to ensure the wave propagates in a region of quasi-homogenous permittivity.

2.3.2 Near-field

In contrast to far-field devices, which avoid direct coupling, near-field devices are designed to exploit tight coupling between close objects. While a near-field device may produce higher usable field strength at working distance than a far-field device,

the characteristics of near-field devices are generally more complicated to analyze.

Two examples of terahertz devices operating in the near-field regime are transmission lines where a sample modifies the propagation constant, and the perturbation of a resonator by a sample.

Transmission lines

The properties of planar transmission lines are somewhat different at terahertz frequencies than microwave frequencies. Effects which may have been negligible, such as radiation loss or substrate modes may become pronounced for certain types of transmission lines operating at terahertz frequencies. The study of the characteristics of transmission lines has become more important for the understanding of fields of study such as integrated circuits, as the search for higher throughput pushes digital logic signal frequencies higher.

Transmission lines designed for terahertz frequencies often have dimensions on the order of tens of micrometers. The dimensions of the lines are chosen to avoid exciting multiple modes. Because of their small size, terahertz transmission lines are often constructed with micro-fabrication techniques such as lithography. Mode confinement and radiation loss are significant problems at terahertz frequencies [22–24]. Radiation can be controlled by several approaches, such as suspending the transmission line on a membrane so its effective permittivity remains close to unity [25], ensuring tight mode confinement in a layered dielectric structure [26], or in the case of coplanar strip line using three strips instead of two [27].

Despite some limitations at terahertz frequencies, transmission lines have strong advantages as broadband systems sensitive to the permittivity of a material under test. Terahertz spectroscopes have been previously proposed using coplanar stripline [28, 29]. Transmission line sensors have a small advantage over resonator sensors in regards to the ability to design a dynamic range for the characteristics of the sources, detectors, and materials used.

Resonator perturbations

The resonant frequency of an electromagnetically resonant structure is related to the permittivity of the materials which form that resonator. If a material to be tested was incorporated into the structure of a resonator, the frequency response of the system would contain information on the permittivity of the sample material under

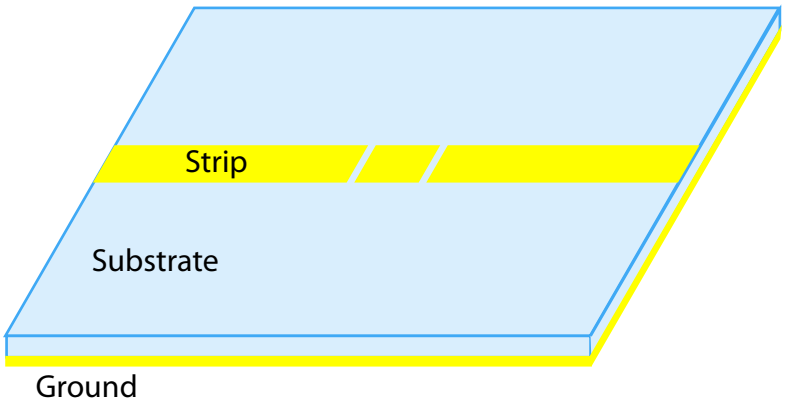

Figure 2.1: A simple example of a transmission line resonator implemented with microstrip.

test. Figure 2.1 illustrates an example of a microstrip transmission line resonator, where the material under test could be applied to the top surface of the substrate, possibly with a thin cover layer to protect the transmission line. A similar apparatus has been used previously as a marker-free system for DNA analysis [30].

Resonators may also be constructed from dielectric shapes, such as a cylinder [31]. Through careful design, the resonator may be made several wavelengths in size at terahertz frequencies to allow for millimeter instead of micrometer scale fabrication. In case of a cylinder large enough to support a host of modes, the wave can travel around the outer edge of the cylinder to constructively or destructively interfere with additional waves on the coupling line. This arrangement is different than the usual microwave case where the cylindrical dielectric resonator is sized to only allow the single fundamental mode to resonate, with all other modes in cutoff.

Another approach is to combine elements of a resonant cavity structure with a free-space optical system [32]. The sample to be sensed is placed on a dielectric rectangular prism resonator coupled to a transmission line. The transmission line is fed by a photomixer, and after passing through the resonator leads to an antenna. An antenna is useful in this apparatus to electrically decouple the transmitter and receiver through the far field. While an antenna is not necessary in this apparatus to isolate the transmitter and receiver, it is the most practical. The alternative would be a ferrite-based circulator, a common microwave component. Ferrite materials and their use in quasi-optical circulators have been demonstrated at terahertz frequencies [33].

As with other near field methods, extracting the measured permittivity of the material under test from the frequency response of the resonant structure depends on

an analytic method appropriate for the test structure. At terahertz frequencies with large bandwidths and a possible tail of a far-infrared absorption process, all materials and the transmission line itself should be assumed to be highly dispersive.

2.4 Human tissue experiments

Given the detailed far-infrared absorption spectra of many materials, terahertz technology has natural applications in biological and medical sensing. Research has been performed to evaluate the suitability of terahertz technologies to identify skin abnormalities [34–37]. This research is generally promising, with findings of good reflection contrast at terahertz frequencies between regions of human skin with basal cell carcinoma and regions without. However, the bulk of terahertz experiments to date have been performed with free-space optical apparatus. While these apparatuses are simple to construct on a lab bench and allow changing elements of the system without disturbing other elements, they are not miniature and are prone to alignment errors.

Part II

Numerical simulation of terahertz systems

Chapter 3

Permittivity models for non-metallic materials

Electric permittivity, commonly represented with ϵ and here treated without regard to non-linear phenomena, is a bulk material property. Rather than comprehensively reviewing the wide variety of literature of theory and experiments on dielectric materials, this section introduces simplified models of select materials for the express purpose of computer simulation of those materials at terahertz frequencies. This restriction allows tractable models to be fit to experimental data at the expense of predicting the behaviour of materials at frequencies beyond the typical far-infrared resonances of many materials.

The main purpose for constructing approximate models for computer simulation is the prediction of dielectric behaviour at frequencies other than where experimentally measured. While some computational electromagnetic codes, typically operating in the frequency domain, strictly do not require the specification of a particular model and can interpolate values from a given data table, other codes, typically operating in the time domain, often require the specification of a model for broad-band evaluation of the behaviour of materials and matched-layer boundary conditions.

This chapter covers select insulators and semiconductors of interest for terahertz technology. Each of the material types is treated in its own section owing to the differences in modeling those materials. Metals are covered in Chapter 4. Where possible the models presented obey physical requirements. This chapter adopts the sign convention for permittivity where a negative imaginary part corresponds to loss. This chapter makes extensive use of the relation between CGS frequency and radian

frequency: $\nu_{\mathrm{CGS}} = \omega/(200\pi c_0)$. Similar to other works, we invoke the standard disclaimer for permittivity modeling: the models given in the following sections are phenomenological in nature.

3.1 Insulators

This section covers the following insulating materials: silica (amorphous silicon dioxide), water, and the polymer bezocyclobutene.

The classic simple harmonic oscillator dispersion relation has been attributed to Helmholtz, Kettler, Lorentz, or a combination of the three.

3.1.1 Silica glass (amorphous SiO_2)

The natural abundance of silicon dioxide is second only to its usefulness in many areas of human arts and technology. Silica glass is an important material for optical components such as lenses and windows due to its transparency across a wide range of frequencies from the far ultraviolet to the mid infrared [38, 39]. While silica glass is less transparent at terahertz frequencies than visible frequencies, silica glass remains useful for terahertz technology due to a balance of manufacturability and sufficiently low loss. However, despite extensive measurements at frequencies from rf to x-ray collected in at least two comprehensive reviews [38, 39], the nature of the permittivity function in silica remains vaguely understood with no consensus. For example, some work assuming silica can be modeled as a disordered charge distribution [40–42] is not cited in the previously mentioned comprehensive reviews.

Regardless of the complexity of the true permittivity function of silica, we may construct a function to approximate the behaviour of silica in the far infrared from a ratio of two polynomials [43]. Aside from numerically stable methods for curve fitting, the form of a ratio of two polynomials was chosen for ease of input to commercial numerical electromagnetic codes. Inspection of the available refractive index and extinction coefficient data from the previously mentioned reviews and other references [42, 44–60] shows at least three resonant processes between 10 and 40 THz. Therefore we specified a model with three sets each of conjugate poles and zeros with a multiplicative constant satisfying causality but not passivity constraints, as follows:

$$\epsilon_r(\omega) = \epsilon_\infty + \sum_{n=1}^{N} \frac{\beta_{0,n} + i\omega\beta_{1,n}}{\alpha_{0,n} + i\omega\alpha_{1,n} - \omega^2}. \tag{3.1}$$

Table 3.1: Simulation parameters in units of rad/s for six-pole, six-zero model of silica glass

Parameter	First	Second	Third
ϵ_∞	2.1028		
α_0	7.1595×10^{27}	2.3496×10^{28}	4.0462×10^{28}
α_1	9.7379×10^{12}	1.1842×10^{13}	1.4896×10^{13}
β_0	3.4658×10^{13}	1.0370×10^{14}	3.8989×10^{14}
β_1	-1.0062×10^{13}	-5.1516×10^{12}	4.7818×10^{12}

The main impurity in the manufacture of silica glass is the hydroxide ion (OH^-). The concentration of hydroxide interacts with the overall permittivity function of a sample of silica glass in several ways, such as the modification of the static permittivity and resonant absorption in near infrared. If the static permittivity can be estimated despite interference from hydroxide contamination [61], then its value may be inserted into Equation 3.1 by means of the Lyddanne-Sachs-Teller relation [43, Eq. 13], which can be re-written as follows to agree with the form of Equation 3.1:

$$\epsilon_\infty = \epsilon_s - \sum_{n=1}^{N} \frac{\beta_{0,n}}{\alpha_{0,n}}. \tag{3.2}$$

To fit the model to the data, we used the `lsqnonlin` function of the Optimization Toolbox in MATLAB. We used the `lsqnonlin` function instead of the `lsqcurvefit` function because not all of the data measured refractive index (or their equivalents) and extinction coefficient at the same frequencies. Because much of the published data is presented as occasionally disjoint sets of refractive indices and extinction coefficients and our chosen model computes permittivity, we chose our objective function as follows:

$$\vec{F} = \begin{bmatrix} n_i - \Re\sqrt{\epsilon_r(\omega_i)} \\ \kappa_i - \Im\sqrt{\epsilon_r(\omega_i)} \end{bmatrix}, \tag{3.3}$$

where n_i and κ_i represent experimentally measured values of refractive index and extinction coefficient, respectively. The qualitative agreement between the data and the fitted curve is very good until approximately 50 THz, where the model predicts the unphysical result that silica becomes a gain medium. The fitted model parameters corresponding to Equation 3.1 are presented in Table 3.1.

Some electromagnetic codes restrict the values of input parameters to non-negative numbers. This restriction does not enforce a passivity restriction on a permittivity

model. As shown in Section 3.2.2, the imaginary part of the permittivity is non-positive everywhere (representing loss) yet a model in the form of Equation 3.1 may still have some negative coefficients. As such electromagnetic codes will not accept the values presented in Table 3.1, some restrictions are required during the curve fitting process. Directly restricting the parameter values to non-negative values produced a model which did not adequately predict either refractive index or extinction coefficient. Given that our purpose is to produce a permittivity model valid for simulations below 2 THz, accuracy above that point is not important. We may reduce the complexity of the problem by disregarding data in the resonant region and by simplifying the model. By inspecting the data, we hypothesize that the behaviour of silica may change at approximately 10 THz. We choose this frequency to cut off experimental data for fitting a model. Next, we choose the standard simple second-order model to fit the reduced data set as follows:

$$\epsilon_r(\omega) = \epsilon_\infty + \frac{(\epsilon_s - \epsilon_\infty)\omega_0^2}{\omega_0^2 + i\omega\delta - \omega^2}, \tag{3.4}$$

where the physical interpretation of the model parameters is:

ϵ_s is the permittivity in the model's low-frequency limit;

ϵ_∞ is the permittivity in the model's high-frequency limit;

ω_0 is the material's resonant frequency;

ω is the angular frequency of the electric field;

δ is the damping frequency of the resonance.

The parameters corresponding to this curve fit are presented in Table 3.2, and the plotted model with experimental data is presented in Figures 3.1 and 3.2 for the refractive index and extinction coefficient, respectively.

The data used for fitting in this Section and illustrated in Figures 3.1 and 3.2 were aggregated from a variety of sources spanning the twentieth century. Equal weight was used for each set of data which may not correspond to the quality of the result. Because the absorption of silica in the infrared is strongly affected by the concentration of impurities, including results from silica manufactured by a technique

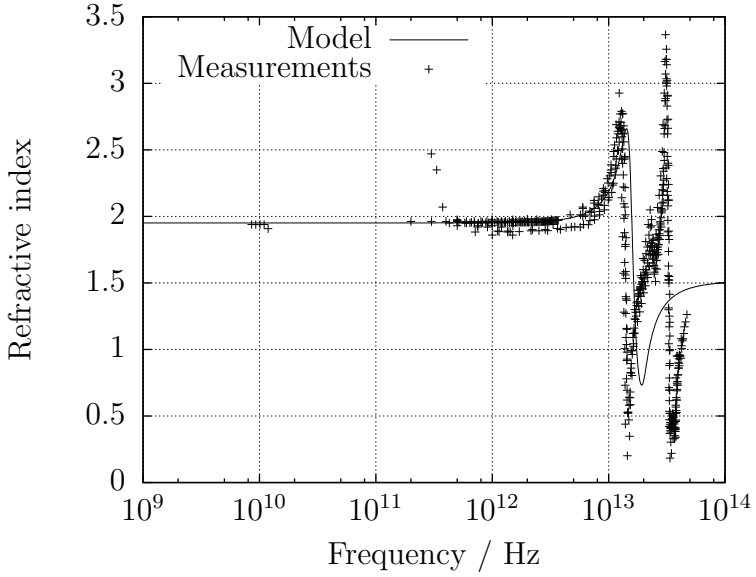

Figure 3.1: Refractive index of silica glass as a function of frequency. Data points are taken from the literature [42, 44–60] and model values are calculated from Equation 3.4 with parameters from Table 3.2

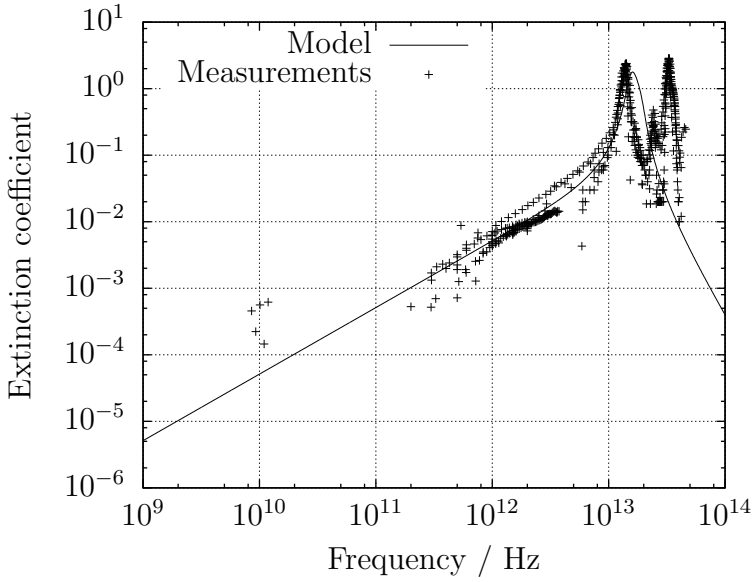

Figure 3.2: Extinction coefficient of silica glass as a function of frequency. Data points are taken from the literature [42, 44–60] and model values are calculated from Equation 3.4 with parameters from Table 3.2

.

Table 3.2: Simulation parameters in units of rad/s for two-pole, two-zero model of silica glass

Parameter	Value
ϵ_∞	2.2921
ϵ_s	3.8073
ω_0	9.7128×10^{13}
δ	1.9823×10^{13}

prone to include impurities may not reflect the quality of a modern sample of silica intended for high-performance applications in optical fibers or other components. The model parameters presented in this Section should be considered an average of all types of silica one may encounter.

3.1.2 Water

The terahertz permittivity of water is of special importance due to the high water content in many plant and animal tissues as well as the atmosphere. The two cases of pure liquid water and water vapour are treated differently. The permittivity of water in the former case may be predicted by a double Debye model [62]:

$$\epsilon_r(\omega) = \epsilon_3 + \frac{\epsilon_1 - \epsilon_2}{1 + i\omega\tau_1} + \frac{\epsilon_2 - \epsilon_3}{1 + i\omega\tau_2}. \tag{3.5}$$

Unlike the generalized model presented for silica, the Debye model has physical interpretations for its parameters given as follows:

ϵ_1 is the permittivity in the model's first low-frequency limit;

ϵ_2 is the permittivity in the model's second low-frequency limit;

ϵ_3 is the permittivity in the model's high-frequency limit;

ω is the angular frequency of the electric field;

τ_1 is the first relaxation time of the polar molecule;

τ_2 is the second relaxation time of the polar molecule.

Table 3.3: Double Debye parameters for pure water

Parameter	Value
First low-frequency permittivity (ϵ_s)	80.528
Second low-frequency permittivity (ϵ_1)	5.2
High-frequency permittivity (ϵ_∞)	3.3
First relaxation time (τ_D)	8.5×10^{-12} s
Second relaxation time (τ_2)	1.7×10^{-13} s

Parameters suitable for use in this model at a temperature of 292.3 K from dc to frequencies of approximately 2 THz [63] in computer electromagnetic codes are presented in Table 3.3.

Because the double Debye model for water only predicts overall permittivity and does not take particular atomic or molecular resonances into account, it is not suitable for predicting electronic resonant behaviour. Precision terahertz experiments require evacuation of the experimental apparatus to prevent unwanted absorption by various atmosphere components [4, Fig. 1].

3.1.3 Benzocyclobutene

Benzocyclobutene (BCB) is an organic polymer with good properties for terahertz technology, such as a relatively low and non-dispersive permittivity and low loss [64]. Unfortunately for those attempting to perform terahertz simulations of BCB structures, no physically derived model has been found satisfactory to explain the permittivity of BCB, including models which fit other polymers [64]. Published data from 0.5 to 5.4 THz can be fit to a model with constant real permittivity and a loss tangent linearly proportional to frequency. This empirical model predicts non-zero imaginary permittivity at zero frequency, which is generally not the case for insulators, and unbounded loss in the high frequency limit, also generally not the case for insulators. To simulate BCB in broadband numerical electromagnetic codes, we require a model which can be expressed in terms of a polynomial ratio.

Table 3.4: General second-order model parameters for BCB

ϵ_∞	α_0	α_1	β_0	β_1
2.3873	4.6357×10^{25}	4.3739×10^{13}	6.0182×10^{24}	3.6605×10^{12}

The general dispersion model presented in Equation 3.1 with $N = 1$ can be expressed as a Taylor series about a chosen frequency ω_0. A set of equations for the real and imaginary parts of the zeroth and first order series coefficients is set up with the intent of solving for ϵ_∞, α_0, α_1, β_0, and β_1. We ignored higher-order series coefficients because their inclusion in the system of equations lead to qualitatively worse solutions than first-order coefficients. We chose to use the `lsqnonlin` function from the Optimization Toolbox of MATLAB to solve this system of equations rather than `fsolve` because we do not require an exact solution, only the closest solution. For the constant parameters we took the average values of given coefficients for the linear fit [64, Table 2] except for "No. 5," which is presumed to be a statistical outlier. We chose the frequency for series expansion to be 1 THz. As expected, the fit is approximate but will serve to qualitatively describe the permittivity of BCB. Parameters for the fitted model are presented in Table 3.4.

3.2 Semiconductors

Models for the permittivity of semiconducting materials at terahertz frequencies are especially important with the widespread modern use of semiconductors to generate terahertz waves as well as electronic technology in general. This section covers permittivity models for gallium arsenide and gallium phosphide.

Table 3.5: Two-pole, two-zero model parameters for gallium arsenide

Material	ϵ_∞	ϵ_0	ω_0 / rad/s	δ / Hz
GaAs	10.86	12.90	5.0859×10^{13}	3.0138×10^{11}

3.2.1 Gallium arsenide

The semiconductor gallium arsenide has great utility in electronic devices and its dielectric behaviour has been extensively studied in the visible through terahertz frequencies. Compared to other materials such as silica glass or even other crystals such as gallium phosphide, as a high-resistivity zincblende type crystal, the far infrared permittivity of gallium arsenide can be sufficiently explained by the two-pole, two-zero model previously given as Equation 3.4 [65]. Parameters for this model are presented in Table 3.5. The behaviour of heavily doped gallium arsenide is not described by this model [66] and is covered in Section 4.2.

The frequency of the infrared absorption resonance is determined to be approximately 8.09 THz by inference from a fit of the model to measurements taken below this resonance [65, 67, 68]. However, a two-pole, two-zero model does not account for the weak multiphonon absorption in pure gallium arsenide observed at 0.4 and 0.7 THz [68]. As mentioned in the introduction to this Part, one instance of a model should not be expected to accurately predict all dielectric permittivity behaviour of a material.

3.2.2 Gallium phosphide

Gallium phosphide is another excellent example of the difficulty of constructing a permittivity model. The commonly accepted model [69, 70] predicts the refractive index of GaP over many orders of magnitude of frequency with accuracy to the fourth decimal place. However, this model underestimates the extinction coefficient by an order of magnitude at 1 THz. While the refractive index data suggests a smooth

Table 3.6: Simulation parameters in units of rad/s for twelve-pole, twelve-zero model of gallium phosphide

$\epsilon_\infty = 1$	α_0	α_1	β_0	β_1
First	4.3036×10^{27}	3.6818×10^{12}	3.4966×10^{26}	9.5582×10^{12}
Second	4.5286×10^{27}	2.1700×10^{12}	8.9537×10^{26}	1.2407×10^{13}
Third	4.7414×10^{27}	6.8448×10^{11}	8.4257×10^{27}	-2.1966×10^{13}
Fourth	2.9840×10^{31}	0	7.6689×10^{31}	0
Fifth	6.4693×10^{31}	0	2.6725×10^{32}	0
Sixth	1.1936×10^{32}	0	1.6591×10^{32}	0

Table 3.7: Simulation parameters in units of rad/s for two-pole, two-zero model of gallium phosphide

Parameter	Value
ϵ_∞	9.0910
ϵ_s	11.147
ω_0	6.8231×10^{13}
δ	1.3270×10^{12}

function, the fine structure evident in the extinction coefficient away from the infrared resonance suggests that a very high order polynomial model may be required.

Notwithstanding the inaccuracy of the extinction coefficient of the commonly accepted model, we present that model in a form suitable for numerical electromagnetic codes working in frequency units of radians per second. Through extensive algebraic manipulation[1], the model may be expressed in the form presented earlier in Equation 3.1 [43]. The coefficients are shown in Table 3.6.

Because some numerical electromagnetic codes will not accept generalized dispersion model parameters less than zero, we performed a fit of the restricted two-pole, two-zero model given earlier in Equation 3.4 to published data below 200 cm^{-1} [69]. Unlike our fit for silica, the present fit was performed with refractive index data only. The static and high-frequency permittivity were fixed values from the same data. Model parameters from the fit are given in Table 3.7.

[1]We suggest the use of a computer algebra system and substituting exact rational numbers for floating point representations (e.g. 11/10 for 1.1).

Chapter 4

Electromagnetic models for metals

In elementary electromagnetic theory, metals are introduced as objects with infinite capacity to conduct current. According to Maxwell's equations a perfect electric conductor excludes time-varying electromagnetic fields. This simplification is of great use in reducing the complexity of problems where the energy absorption or finite permittivity of the metal has little effect on the outcome of the problem. However, in certain cases the nature of the metal object must be considered for accurate analysis. For instance, the surface wave effect known as the surface plasmon polariton cannot be modeled with a perfect conductor. Surface plasmons are not a solution of the wave equations if the metal is a perfect conductor. Realistic analysis or computer simulations of the interaction of electromagnetic waves with metal objects requires accurate, physically based models of the behaviour of metals.

Two approaches to modeling energy absorption and field penetration are the surface impedance method and free electron models. The former is a convenient simplification which only models energy absorption and not field penetration. The surface impedance model has somewhat complex criteria to determine its suitability to a particular problem and is detailed in Section 4.1. A free electron model which models a

metal as material which supports an internal electric field is valid for all frequencies except those disclaimed by the particular model. Usually, this termination is in the range of visible light. The Drude model, a common free electron model, is detailed in Section 4.2.

To illustrate the important differences in selection and use of the surface impedance and Drude models, we include a comparison in Section 4.3. We compare theoretical and simulation results for rectangular waveguide and coplanar stripline transmission lines. Rectangular waveguide was chosen for computational and theoretical tractability and coplanar waveguide was chosen because of the influence on evaluation of the candidate devices for terahertz spectroscopy in Chapter 6.

4.1 Surface impedance model

The surface impedance model is based on the approximation of a metal being a good conductor, which can be stated in three equivalent ways: the electromagnetic wave impedance inside a good conductor is far less than the wave impedance of free space, the imaginary part of the permittivity is much greater than the real part, or the conductivity is much greater than the product of radian frequency and permittivity. This assumption allows the simplification of the integral formulation of Poynting's theorem, incorporating terms depending on the properties of both sides of the material interface, into an integral depending solely on the properties of the metal and the tangential magnetic field on the metal. From [71], the power converted to heat through an area S of a metal object is given by:

$$P = \frac{R_s}{2} \int_S |\vec{J}_s|^2 ds = \frac{R_s}{2} \int_S |\vec{H}_t|^2 ds, \tag{4.1}$$

where the surface resistance is given by

$$R_s = \sqrt{\frac{\omega\mu}{2\sigma}}. \tag{4.2}$$

A full derivation of the preceding equations is available in [71].

Because the surface impedance model allows calculation of power loss without consideration for fields inside the metal object, some analysis, especially by computer simulation software, avoids calculating these fields. This simplification greatly speeds computation in cases where the skin depth of the metal is much smaller than the mesh step. As stated by Pozar [71, p. 38]:

> This method is very general, applying to fields other than plane waves, and to conductors of arbitrary shape, as long as bends or corners have radii on the order of a skin depth or larger.

The preceding criteria for applicability of the surface impedance model excludes some cases of interest in modern technology. Some microwave devices, for example monolithic microwave integrated circuits, may have planar metal features a skin depth thick or less depending on operating frequency. The surface impedance model assumes that each metal face extends to infinity, greatly limiting accuracy in such a case. In the case of enclosed metal waveguide this assumption is much more valid as the waveguide walls are often constructed very many skin depths thick for structural stability. If the surface impedance model is not applicable to a problem due to thin planar conductors or surface features, a free electron model may be a better choice.

4.2 Drude model

In 1900, Paul Drude published his model for electronic behaviour in solid state metals [72, 73], hereafter referred to as the "Drude model." The Drude model applies to metals or semiconductors with sufficient free charge where the electrons may be considered as a gas colliding with stationary atoms. The model accurately predicts the behaviour of metals such as aluminum, gold, lead, and copper, but not metals such as iron, cobalt, or nickel [74]. The model also accurately predicts the behaviour of some strongly doped semiconductors, such as N- and P-type gallium arsenide [75].

In contrast to the surface impedance model, which does not require evaluation of the fields inside a metal, the Drude model can be used to calculate the fields inside a metal object. The permittivity of a metal predicted by the Drude model is given by:

$$\epsilon_r = \epsilon_\infty - \frac{\omega_p^2}{\omega(\omega - iv_c)}, \tag{4.3}$$

where:

ϵ_r is the relative permittivity of the metal;

ϵ_∞ is the permittivity in the model's high-frequency limit;

ω_p is the metal's electron plasma frequency;

v_c is the electron collision frequency;

ω is the angular frequency of the electric field.

Ordal et al. provide parameters for the Drude model inferred from curve fits of a host of experimental measurements of various metals [74]. However, those parameters were acknowledged to be inferred from eyeball fits of the data. Presumably, the parameters were eyeball fit to avoid performing a computationally intensive non-linear least-squares fit with complex numbers. This specific case of a curve fitting problem has been treated [76, 77], but design and implementation of a non-linear least-squares

system is beyond the scope of this work. We have taken the experimental data from [74] and used the function `lsqcurvefit` of the commercial software MATLAB to perform a non-linear least-squares fit.

When fitting Equation 4.3 to a set of data there are three free parameters of the model that may be adjusted: ϵ_∞, ω_p, and v_c. To enable a fair comparison, presented in Section 4.3, between the Drude and surface impedance models, we modified the Drude model to fix one parameter with conductivity. Regardless of the result for the free parameters, the models will then provide identical results in the low-frequency limit. We chose to fix the plasma frequency for algebraic convenience. To avoid transcription error we chose to work in the same CGS units as the original data. The conductivity σ, in units of cm^{-1}, can be expressed in terms of the plasma and damping frequencies as follows:

$$\sigma = \frac{\omega_p^2}{4\pi\omega_\tau}\mathrm{cm}^{-1}. \tag{4.4}$$

To import conductivity from the SI world, we can convert to CGS with the following equation where ρ_0 is in SI units of $\Omega \cdot \mathrm{m}$:

$$\sigma = \frac{c_0}{2 \times 10^9 \pi \rho_0}\mathrm{cm}^{-1}. \tag{4.5}$$

Note that constants have been combined, and that the constant is an exact integer and not a truncated decimal.

As discussed further in the following subsection, the high frequency dielectric constant is often assumed to be unity for the Drude model. If one wishes to fix the real part sign crossover frequency, the following equation may be substituted into the

Drude model to eliminate an additional parameter:

$$\epsilon_\infty = \frac{\omega_p^2}{\omega_\tau^2 + \omega_c^2}, \tag{4.6}$$

where ω_c is the experimentally determined sign crossover frequency. If both Equations 4.6 and 4.4 are substituted into Equation 4.3, then the model is left with one free parameter to fit.

4.2.1 Drude model for gold

Gold is a valuable conductor for electronic circuits due to its very high conductance, malleability, and resistance to corrosion and oxidization. The permittivity of gold has been widely studied over the twentieth century and has previously been fit to a Drude model [74]. The permittivity of gold has been measured over a very wide range of frequencies as shown in Figure 4.1: [78–86].

The Drude model parameters for gold given by Ordal et al. [74] and the fitting procedure in Section 4.2 are presented in Table 4.1. The real and imaginary parts of the relative permittivity predicted by the original curve fit, our joint least squares fit on the real and imaginary data, and experimental data from [74] and [78] are presented in Figure 4.1. Figure 4.1 shows the discrepancy between the original curve fit and our fit and illustrates the non-Drude behaviour of gold above approximately 300 THz. Broadband free-electron models of gold must include additional parameters to model gold accurately in the ultraviolet wavelength range [87].

Table 4.1: Comparison of previously published Drude model parameters and least-squares fit

Parameter	Ref. [74]	Least-squares
Plasma frequency / cm^{-1}	7.25×10^4	6.638×10^4
Damping frequency / cm^{-1}	2.16×10^2	1.627×10^2
High frequency dielectric constant	1.00	1.889

Measurements of the permittivity of gold at beyond approximately 300 THz show significant discrepancies to the Drude model. This frequency range is far beyond the operating frequency of the devices in this work except for determining an appropriate high frequency dielectric constant for the Drude model. The anomalous behaviour of gold at high frequencies is theorized to be due to electronic interband transitions, which partially account for the gold colour of gold metal. Extensions to the Drude model have been proposed to account for this anomalous behaviour [87].

From experimental observations of the permittivity of gold, we see that the real part of the permittivity will change sign at approximately 1.45 PHz, or 207 nm. Equation 4.3 suggests the real part of permittivity will also change sign, but from plots of experimental data and Drude predictions we observe that the Drude model significantly deviates from observations in this region. Despite this observation, we can determine a fictional high frequency dielectric constant to place the sign change at the appropriate frequency. Choosing a high frequency dielectric constant other than one is actually a trade-off between two goals: approximating the dielectric function at the sign crossover frequency, and acknowledging that the measured dielectric response of many materials approaches vacuum conditions in their high frequency limits.

4.3 Comparison of surface impedance with Drude models

To illustrate the difference in results and usage for the surface impedance and Drude models, we present calculated and simulation results for rectangular waveguide and coplanar stripline made from gold from the commercial software CST Microwave Studio 2010. Rectangular waveguide was chosen for computational and theoretical tractability and coplanar waveguide was chosen because of the influence on evaluation

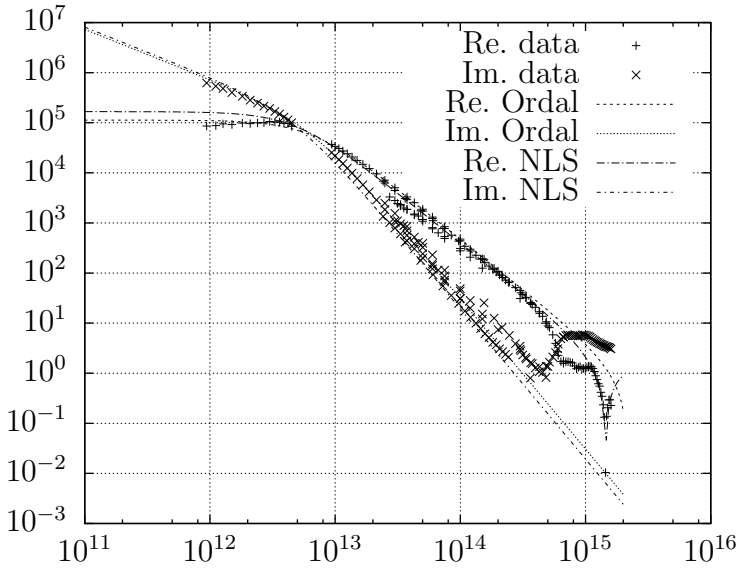

Figure 4.1: Real and imaginary parts of permittivity of gold. Experimentally measured values are taken from the literature [78–86], and Drude model parameters are taken from Table 4.1, where "NLS" refers to our curve fit by the non-linear least squares method.

of the candidate devices for terahertz spectroscopy presented in Chapter 6.

To begin the comparison, in Figure 4.2 we present the skin depth coefficient for gold calculated by two methods. The first assumes the metal is a good conductor, and the second uses the electric permittivity predicted by the Drude model. We assume gold has dc conductivity of 4.52×10^7 S/m [88], and has the Drude parameters presented in Table 4.1. Because the conductivity and Drude approaches give similar results for low frequencies, we hypothesize that unless the problem requires consideration of effects only predictable with free electron models, the surface impedance model will give similar results to the Drude model.

For utmost accuracy, one could include the measured dc value of magnetic permeability for gold. Some results in research on magnetic permeability are reported in the CGS system of units. Care must be taken when converting values from CGS to SI systems due to differing definitions of physical constants [89]. The specific case

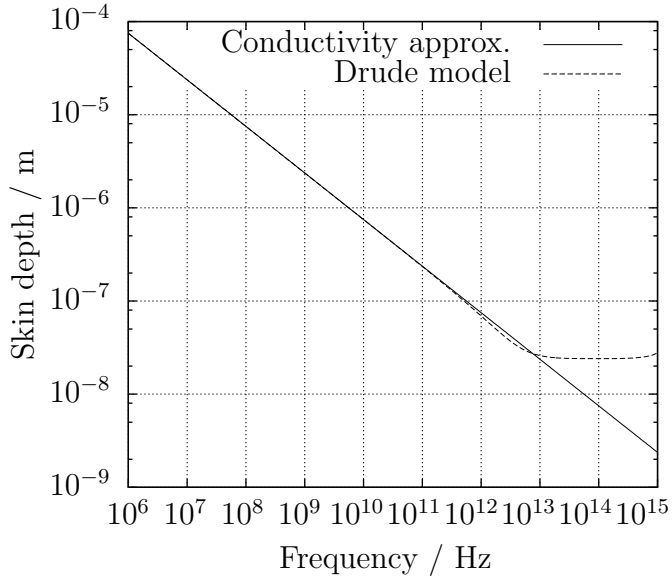

Figure 4.2: Comparison of skin depth calculated by Drude model and conductivity approximation for gold.

of magnetic mass susceptibility measured in units of emu per cubic gram can be converted to the common SI unit of volume susceptibility by the following relation:

$$\chi_{v,\mathrm{SI}} = 4\pi\rho\chi_{m,\mathrm{CGS}}. \tag{4.7}$$

The susceptibility of pure gold at 295 K was measured to be -0.1430×10^{-6} emu/g^3 [90], which is equivalent to 3.468×10^{-5} (dimensonless) in SI, assuming gold has a density of 19.30 g/cm^3. Simulations performed in CST Microwave Studio 2010 with this value of susceptibility showed negligible difference to simulations performed with a susceptibility of zero.

4.3.1 Comparison using rectangular waveguide

Rectangular waveguide is an attractive technology for many theoretical and practical purposes. Rectangular waveguide is defined by a single closed rectangular conductor,

bounding theoretical calculations and numerical simulations. The closed nature of the problem is arguably more important for computer simulation. Several simulation techniques in both time and frequency domain simulations are less accurate or stable in open problems. The most notable example is absorbing boundary conditions which are only absorbers of the continuous wave equation and must produce a minimal reflection when discretized. Therefore, simulation of rectangular waveguide with surface impedance and Drude model walls is an attractive test case to determine whether commercial electromagnetic simulation software is capable of simulating these models.

We chose a rectangular waveguide with dimensions 254 micrometers wide and 127 micrometers tall to ensure the working bandwidth, between 0.75 and 1.1 THz, of the waveguide included our proposed spectroscope's design frequency of one terahertz. The walls were 2 micrometers thick and terminated by an electric boundary condition. The simulation was 300 micrometers in length. The waveguide was simulated with CST Microwave Studio 2010 using the time and frequency domain solvers with hexahedral and tetrahedral mesh. CST Microwave Studio supports hexahedral mesh for the time domain solver and hexahedral and tetrahedral mesh for the frequency domain solver. Unfortunately, the frequency domain solver with hexahedral mesh does not support the surface impedance model.

Hexahedral mesh with time domain solver

For hexahedral mesh with time domain solver, CST Microwave Studio 2010 supports objects with surface impedance boundary as well as Drude model.

Hexahedral mesh with frequency domain solver

For hexahedral mesh with time domain solver, CST Microwave Studio 2010 supports objects with Drude model only.

The automatic hexahedral mesh engine in CST Microwave Studio 2010 did not produce an acceptable inital mesh for study of the Drude model. The initial mesh was too dense in the vacuum-filled center and too sparse in the region immediately in front of and behind the waveguide walls where the field is expected to change rapidly in space. We overrode the automatic mesh system with a manual mesh started from an automatic mesh which only considered highest simulated frequency. We invoked the frequency domain solver iteratively, adding one mesh line half the distance from the previous one per iteration. We also inserted additional mesh lines in the free space region of the waveguide one run after beginning the procedure to avoid over-meshing free space where less rapid field changes were expected. We terminated the mesh line insertion procedure when the change between simulated propagation loss iterations changed by less than 0.01%. The change in error is illustrated in Figure 4.3, where the data points represent the relative change between the previous simulation and the simulation at that mesh density. The skin depth of gold at a frequency of 1 THz is approximately 75 nm calculated using a conductivity of 4.52×10^7 S/m. Figure 4.3 shows the relative change between 125 and 62.5 nm to be approximately 8.5%, which may not be acceptable for some applications.

Tetrahedral mesh with frequency domain solver

For tetrahedral mesh with frequency domain solver, CST Microwave Studio 2010 supports objects with surface impedance model only.

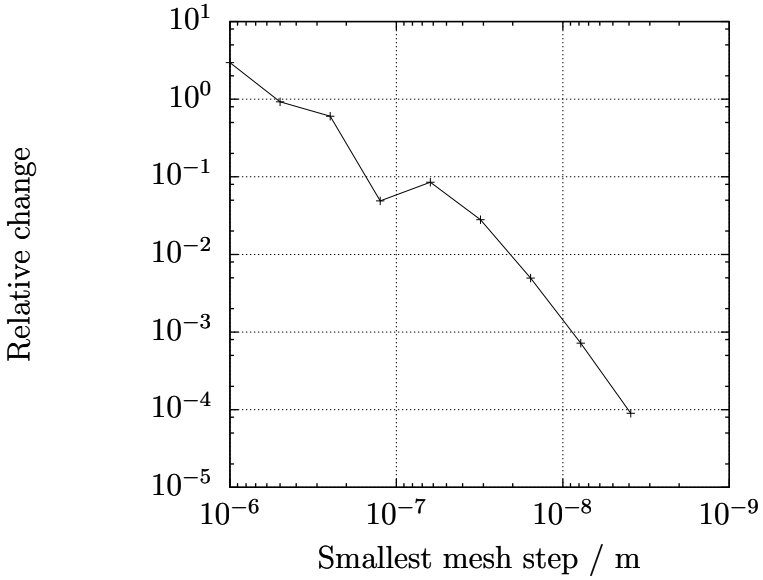

Figure 4.3: Run-to-run change of propagation loss simulated by CST Microwave Studio 2010.

Comparison of numerical solvers with surface impedance theory

To calculate the conductor loss in rectangular waveguide we follow the perturbation approach in Pozar [71]. The surface current on each wall may be calculated from the magnetic field, and that surface current is substituted in Equation 4.1 where the surface integral is changed to a contour integral to yield loss per unit length. The conductor loss for the TE_{10} mode is given by:

$$\alpha_c = \frac{R_s}{a^3 b \beta k \eta}(2b\pi^2 + a^3 k^3), \tag{4.8}$$

where R_s is the surface resistance from Equation 4.2, k is the plane wave propagation constant in the dielectric material filling the guide, a and b are the guide width and height, η is the wave impedance in the material filling the guide, and β is the propagation constant of the TE_{10} mode. Equation 4.8 is plotted in Figure 4.4 along with three sets of simulation results from CST Microwave Studio 2010.

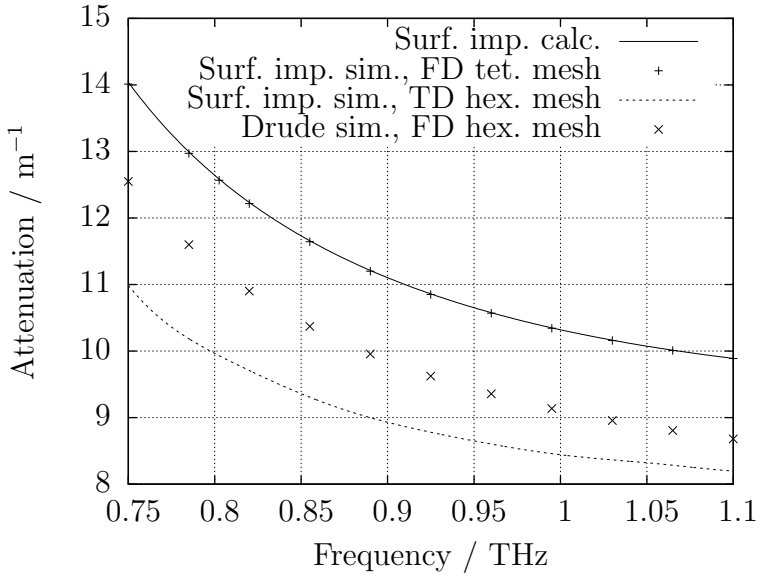

Figure 4.4: Comparison of field loss per unit length in rectangular waveguide calculated by several methods

Figure 4.4 shows that CST Microwave Studio 2010 frequency domain solver with tetrahedral mesh agrees with the surface impedance theory. We cannot explain the difference with the time domain solver, which has simulated 20.2% error compared to the frequency domain solver. The frequency domain solver with hexahedral mesh simulating the Drude model also generated different results. The surface impedance model only considers power lost as a plane wave propagating normally into the metal to infinity. This excludes the small cross-sectional waveguide corner areas of the simulation, which were observed to have volume current density of at most 8.86×10^9 A/m^2. Additionally, the simulated current density displayed a singularity at the interface between waveguide dielectric and Drude metal. Although the mesh density was increased until the loss per unit length changed less than 0.01%, the volume current singularity could introduce numerical error into the simulation. In addition to theoretical error due to waveguide corner volume current density and a different surface resistance due to the Drude model, these two sources of error could explain the discrepancy between Drude and surface impedance model simulations.

4.3.2 Comparison using stripline

From a perspective of complexity of electromagnetic analysis, coplanar stripline can be more difficult to analyze than other types of transmission lines. Coplanar stripline is open, unlike rectangular waveguide, with fields mathematically extending to infinity. Coplanar stripline only supports quasi-TEM propagation in practice due to the finite thickness substrate, unlike enclosed stripline which supports TEM propagation. Due to these problems and others, analysis of coplanar stripline often involves approximations, assumptions, and numerical methods.

The main difficulty in computing the propagation loss coefficient for coplanar stripline is the difficulty in evaluating the surface current, which has singularities at

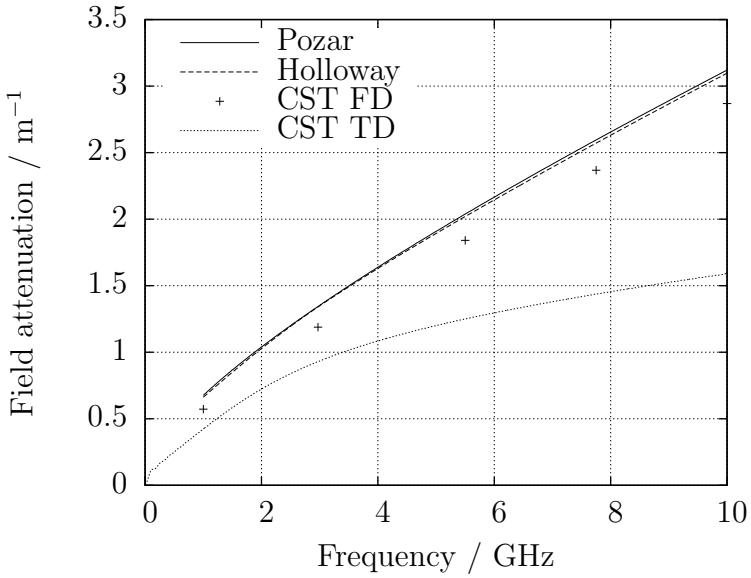

Figure 4.5: A comparison of field attenuation predictions for enclosed stripline by Pozar, Holloway, and CST Microwave Studio 2010.

each edge in coplanar stripline. As treated by Holloway, the integral may be modified by reducing the limits of integration to avoid divergence and introducing a correction factor [91]. To validate this approach we compared the theory from [91] for enclosed stripline with textbook results from Pozar [71] and simulation results from CST Microwave Studio 2010 using the time domain solver with hexahedral mesh and frequency domain solver with tetrahedral mesh. We chose stripline to begin the comparison because of its TEM propagation, natural ground plane boundaries, and insensitivity to electric side boundaries due to two-axis symmetry in the propagation direction. Additionally, Reference [91] includes a comparison with experimental measurements by others, lending credibility to their theory at gigahertz frequencies.

Figure 4.5 compares field attenuation coefficient calculated and simulated by four methods. Loss calculated by Pozar's theory includes center conductor and dielectric loss, but not ground plane conductor loss. Loss calculated by Holloway's theory includes center conductor, dielectric, and ground plane conductor loss. The simulation

results from CST Microwave Studio 2010 frequency domain solver with tetrahedral mesh are 9.8% lower than Holloway's theory. The time domain solver in CST Microwave Studio 2010 does not directly calculate propagation loss for waveguide ports so the loss was calculated from the measure of total power lost in the simulation volume. This result was significantly lower than the other three results, although the curve has the appearance of the same functional form as the other results. The time domain solver in CST Microwave Studio 2010 produced different results than other methods in the previous subsection, illustrated in Figure 4.4.

Chapter 5

Simulation method

Discrete-time and space simulation of electromagnetic problems is often not straightforward and requires consideration of the nature of the problem and the capabilities of the particular computer program used to simulate the problem. A computer program may not be accurately computing the problem posed to it, and the problem posed to it may not be an accurate approximation of the desired problem. These considerations are often coupled and may require specialized simulation test cases to demonstrate the ability of a particular algorithm to solve a given problem.

Workers in the field of computational electromagnetics have created a wide variety of numerical methods for solving electromagnetic problems, such as finite-difference time-domain, finite integration technique, method of moments, and others. Choosing a numerical method requires consideration of the nature of the problem and the capabilities of some possible solvers. In the present case of planar terahertz structures with radiation losses, we desire a solver which can simulate the magnitude and phase transfer characteristic between an input and output of the device while accounting for radiation, dielectric, and conduction loss.

5.1 Software comparison

We evaluated several simulators for suitability for simulating planar terahertz structures, including Ansoft HFSS 11, Sonnet em, and CST Microwave Studio 2010 (MWS). Each of these programs is mature with diverse capabilities, advantages, and disadvantages. These programs are sufficiently different that comparing them in a table does not allow for important subtleties.

5.1.1 Ansoft HFSS

HFSS is a mature, extremely capable tetrahedral mesh finite-element method frequency-domain simulator. HFSS allows the user to define a wide array of boundary conditions conformal to the structure, such as electric, magnetic, and two types of absorbing boundary. The ability to tailor the electromagnetic parameters and shape of an absorbing boundary is unique among the simulators compared here. HFSS has an advanced facility for additional calculations on electric or magnetic fields, such as computing the dot product, cross product, divergence, curl, and other operations.

5.1.2 Sonnet em

Sonnet em is an exceptionally fast frequency domain simulator, but is limited to planar simulations with electric boundary conditions. All dielectric layers are considered to extend to the boundaries. Because many structures designed to operate at terahertz frequencies must be constructed with planar fabrication techniques, we can take advantage of the limitation of only solving planar structures. However, the mandatory electric boundary conditions do not allow study of the radiation effects which significantly impair terahertz transmission line performance. The software uses the method of moments to produce results. Sonnet em does not excite a structure by

waveguide ports like HFSS and MWS, so visualization of port modes is not possible.

5.1.3 CST Microwave Studio

CST Microwave Studio provides time-domain and frequency-domain simulators. While MWS provides a diversity of solvers, mesh types, excitation types, field monitors, and material types, not all styles of the preceding are available with each solver, making comparison between simulation methods difficult. CST Microwave Studio 2010 includes a time-domain solver, general-purpose, resonant, method-of-moments, and eigenmode frequency-domain solvers. The time-domain solver is restricted to hexahedral mesh, but the general-purpose frequency-domain solver may use either hexahedral or tetrahedral mesh. MWS enforces a rectangular prism boundary on the simulation except in the special case of a structure encased in PEC simulated by the frequency-domain solver with tetrahedral mesh.

MWS supports periodic boundary conditions, which can turn the greatest weakness of discrete space simulation, truncation, into a powerful asset. An approximate termination of the problem is changed to an exact infinite expansion of the problem, which may or may not be applicable to a given structure. This feature was investigated to improve the accuracy of simulation of coplanar stripline by allowing the radiation from periodic copies of a transmission line to superimpose. In this approach the radiation was observed to be perpendicular to the plane of the transmission line. This was hypothesized to improve absorbption by the open boundary condition, which perfoms optimally when fields are parallel to the boundary plane, by eliminating dependence on one simulation coordinate. No improvement was observed, and the simulation volume was greatly increased to avoid coupling between periodic copies of the transmission line [24].

5.2 Software selection

Our criteria for selecting a commercial software program to simulate terahertz structures is the ability to accurately simulate the propagation and radiation from diverse three-dimensional structures. While the structures reviewed in Chapter 6 are planar, Sonnet em is disqualified because of its limited capabilities for complex structures and radiation phenomena, leaving Ansoft HFSS and CST Microwave Studio. We choose CST Microwave Studio 2010 to simulate terahertz structures because of its ability to cross-check results with time and frequency-domain solvers and different meshes.

5.3 Simulation of coplanar stripline at terahertz frequencies

Both CST Microwave Studio and Ansoft HFSS feature a special simulation boundary condition called a waveguide port. This feature performs an eigenmode calculation on the surface of the waveguide port and excites the simulation with the calculated field patterns. Unfortunately, a model of coplanar stripline on an electrically thick dielectric causes both simulators to treat the port as a dielectrically loaded waveguide perturbed by the quasi-TEM coplanar stripline mode. We considered several methods for performing an accurate simulation: transmission line section, excitation by discrete port, restriction of mode calculation frequency, and TEM mode launcher.

5.3.1 Transmission line section

The most straightforward method for simulating the loss and phase delay per unit length of coplanar stripline is to construct a section of transmission line and measure the transfer properties of the section. This method has the advantage of neglecting the

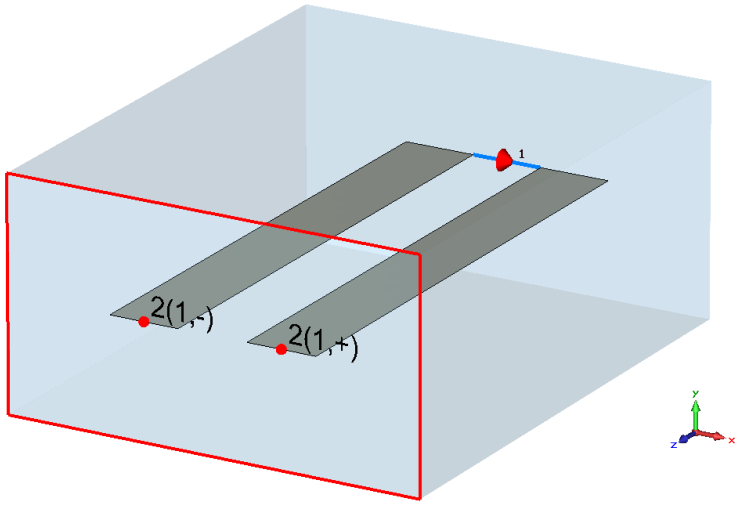

Figure 5.1: Isometric view of a coupling structure between a discrete port (point source) and coplanar stripline terminated in a waveguide port.

influence of the source and detector. Neglecting the source and detector simplifies the design of the transmission line. Unfortunately, measurement using the transmission line section approach is prone to several sources of error at terahertz frequencies.

5.3.2 Excitation of coplanar strip line by discrete port

A natural choice for exciting a coplanar stripline simulation is a point source, where the excitation occurs between two mesh steps. Semiconductor photomixers have approximately the same structure. We designed a test simulation in CST Microwave Studio, depicted in Figure 5.1, to measure the characteristics of this configuration. In this simulation, a discrete port (point source) drives a coplanar stripline terminated by a waveguide port. The computation domain is filled with vaccuum and symmetric about the y–z and x–z planes, where the coordinate directions are defined in Figure 5.1. This configuration was chosen to study the discrete port feed mechanism without the influence of a dielectric substrate.

The bounding box of the simulation was 120 micrometers wide, 65 micrometers

tall, and 150 micrometers long. The coplanar strips were 20 micrometers wide and separated by 20 micrometers. These dimensions were chosen to cause the discrete port, set to the same characteristic impedance as the transmission line, to couple to the fundamental mode of the coplanar stripline and not to waveguide modes. The rear wall of the simulation where the discrete port is located is a magnetic wall boundary condition. The front wall is a waveguide mode boundary condition, and the remaining walls are electric boundaries. The notation of "2(1,+)" in Figure 5.1 refers to waveguide port two, first multipin port group, positive terminal. Multipin waveguide ports were used to force CST Microwave Studio to consider the waveguide housing at a floating potential relative to the coplanar stripline.

Because the simulation contains no radiation boundaries or lossy materials the S parameter matrix should be symmetric. Figure 5.2 is a Smith chart of the input reflection coefficients from the discrete port (numbered one) and waveguide port (numbered two). We see these curves are not identical, possibly due to differences in the tetrahedral mesh structure surrounding each port. We also see that the reflection coefficients track the resistive match line on the inductive side of the chart. This is consistent with self-inductance from the small wires connecting the discrete port to the transmission line.

We conclude that excitation by a discrete port is not an optimal method for simulating the fundamental propagating mode on coplanar stripline due to discrete port self-inductance and excitation of a continuum of free-space modes, which may interfere with simulation measurement through reflection from the structure or radiation boundary conditions.

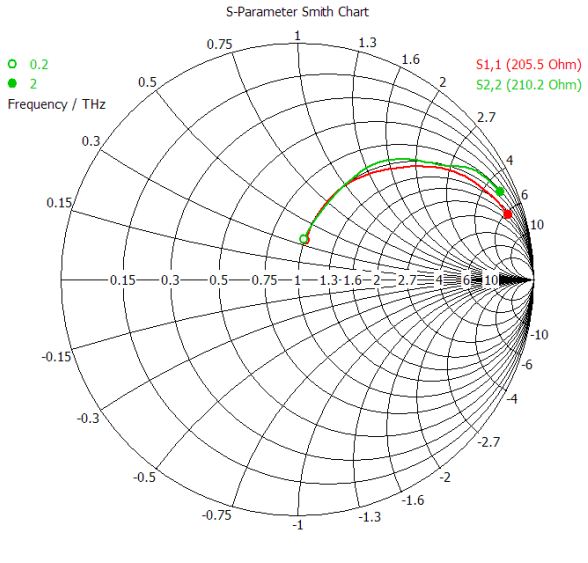

Figure 5.2: Smith chart illustrating the high reflection coefficient of the coupling structure, likely due to self-inductance from the wires connecting the discrete port to the coplanar line.

5.3.3 Restriction of mode calculation frequency

The eigenmodes of any transmission line inhomogeneously filled with dielectric change with frequency. Some time-domain computer simulation software allows the user to choose one frequency for mode calculation. The simulated reflection coefficient is influenced by the congruence of the waveguide mode to the normal modes of a simulated structure. If the mode solver cannot reproduce these modes accurately, power will be reflected from inside the simulation, which cannot be completely absorbed due incongruence of the calculated port mode, which may reflect again into the structure, and so on.

As of this writing, commercial software calculates the eigenmode of a coplanar stripline on a thick dielectric substrate as a superposition of the normal coplanar stripline mode and a dielectric loaded waveguide mode. However, this effect is frequency-dependent and is not significantly in error at gigahertz frequencies. Therefore, we may take advantage of the feature in CST Microwave Studio time-domain

solver to calculate the coplanar stripline mode at a frequency low enough to arbitrarily be judged free of the loaded waveguide mode.

5.3.4 TEM mode launcher

The final approach considered for simulation of complex propagation coefficient in covered coplanar stripline is the TEM mode launcher. The TEM mode launcher is an additional structure placed within the simulation for two purposes. The first is to present a homogeneous port environment to the waveguide port solver. If the waveguide port solver has difficulty separating a loaded waveguide mode from the coplanar stripline mode, one solution is to remove the inhomogeneity. The next purpose is to convert the TEM coplanar stripline mode to a quasi-TEM mode with maximal power transfer to the quasi-TEM mode. A converter designed for minimal reflection may accomplish that goal at the expense of large scattered fields, but a converter designed for maximal transmission will minimise scattered fields.

5.3.5 Constant permittivity buffer to open boundaries

If the commercial electromagnetic code of the user's choice does not support dispersive and/or lossy materials adjacent to a radiation boundary, a buffer zone may be created in the simulation volume. The permittivity of this buffer zone should be chosen to minimize reflection due to radiation from the proposed covered transmission line. The direction of this radiation changes with frequency.

This buffer zone should be assigned a permittivity equal to the real part of the dispersive material at the most sensitive frequency. In the case of the proposed covered transmission line, this frequency is the highest frequency considered for simulation, which is subject to the highest radiation loss.

5.4 Numerical methods for measuring loss

Many numerical electromagnetic codes provide features to measure the scattering parameters of a simulated structure. This measurement is straightforward if the code allows waves to be sourced and sunk through waveguide ports matched to the simulated structure. However, measuring the scattering parameters of a coplanar stripline with open boundary conditions is not straightforward.

The first problem results from forcing the code to calculate the waveguide mode at a particular frequency to avoid exciting fictitious substrate modes as described in Section 5.3.3. The electromagnetic field distribution of an inhomogeneous transmission line generally changes with frequency, so if the field distribution of the simulated waveguide port is static then the simulated transmission line is not matched to the waveguide port.

The second problem relates to the radiated waves from the transmission line. A traveling wave on an inhomogeneous transmission line will generally lose power by radiation into the region with higher permittivity. Because the radiation from a transmission line is continuous along the length of the line, there will always be some radiation released at an angle [23] which will intersect an edge of the simulated waveguide port. Decreasing the depth of the waveguide port in the substrate is not an option because the waveguide port must be large enough to avoid perturbing the calculation of the travelling mode. Because the propagation constant of the radiated wave is equal to the plane wave propagation constant in the higher permittivity material and not the effective permittivity of the guided wave on the transmission line, the radiated wave will interfere with the guided wave on the simulated waveguide port face in a frequency-dependant manner.

Given these two problems, we propose a method in simulation for measuring phase change and attenuation along a transmission line using an array of field probes.

The location of the probes in the plane transverse to the direction of propagation is important. The probes should be placed in the location with no radiation in the direction of propagation. For example with a planar transmission line, placing the probes in the substrate would record both the guided wave and the radiated wave. Placing the probes in the plane of the transmission line along the direction of propagation will only record the guided wave, because any radiation would be immediately coupled back into the guided wave. We may form the time-averaged Poynting vector to determine which field components we must record:

$$P_z = \vec{P} \cdot \vec{z} = \frac{1}{2}\Re\{E_x \bar{H}_y - E_y \bar{H}_x\}, \tag{5.1}$$

where the bar denotes complex conjugation, z is a unit vector in the propagation direction, E and H are the electric and magnetic fields, and $\Re$ is the real part operator. If the probes are deployed along a simulation symmetry condition we may discard one of the terms in the preceding equations, depending on the nature of the symmetry.

If we assume that the shape of the wavefront transverse to the propagation direction is constant at each frequency, then the power at a given point z along the direction of propagation is given by

$$P(z) \propto \exp(-2\alpha z), \tag{5.2}$$

where α is the field loss coefficient. We can take the power at two different points z_1 and z_2 and solve the equations for α as follows:

$$\alpha = -\frac{1}{2(z_2 - z_1)} \ln \frac{P(z_2)}{P(z_1)}. \tag{5.3}$$

Unfortunately, one cannot simply make two measurements by experiment or simu-

lation and apply Equation 5.3. Experimental or simulation error manifests in many forms. One source of error familiar to users of time-domain numerical electromagnetic codes is oscillation in time signals due to truncation of the simulation process, equivalent to convolution with a rectangle function. Regardless of the source of error, we require a method to obtain a robust estimate for α.

We hypothesize that the main sources of error in a measurement of α in time-domain simulation could be truncation of time response, numerical error in propagating the excitation signal, reflection from an imperfect radiation boundary, diffraction effects from the edge of the waveguide port not covering an entire simulation wall, and many other sources. These errors are not normally distributed and are likely correlated with position in the simulation. Under these conditions, ordinary least squares is biased and is not a maximum likelihood estimator for α. We propose the use of minimum absolute deviation as a robust estimation technique, implemented using iteratively re-weighted least squares.

The lower limit on the number of probes required to obtain an accurate estimate of α is the Nyquist rate for the highest expected spatial frequency along the direction of propagation. Inversely, the minimum required sampling interval for a wave with time frequency f and refractive index n is

$$D < \frac{c_0}{2fn}, \tag{5.4}$$

where c_0 is the speed of light. For insurance against undersampling, choose the highest value for refractive index, which would be the higher of the substrate and superstrate permittivities for a typical planar transmission line.

Determining the true highest time frequency in a time-domain simulation requires obtaining the raw signal that a particular code will excite a structure with and inspecting its discrete Fourier transform. For example, if a particular code is asked to

excite a structure with frequencies up to 2 THz, it may generate a signal with frequencies up to 5 THz or beyond to ensure sufficient energy in the pulse in the desired frequency range. For a simulation of length L, the minimum number of probes is given by $N > \lceil L/D \rceil$.

5.5 Comparison of simulation to experimental results

To ensure that our simulation method is realistic, we may simulate previously published transmission line results to check against theories of radiation [23] and conduction loss [91]. Coplanar stripline is difficult to analyze due to infinite bounds, typically heterogenous cross section, and singularities of integration for surface current. The transmission line considered for this comparision had the following dimensions: width of the lines was 30 μm, spacing was 20 μm, substrate relative permittivity was 10.5, and the simulation length was 1000 μm. We perfomed a simulation of a transmission line loss with the preceding parameters in CST Microwave Studio, and calculated expected values for a line with those parameters according to the radiation and conduction loss theories. Figure 5.3 illustrates the results of the two computations. While the simulation does not exactly match the loss theories in magnitude or shape, it does show the high-frequency loss local maximum and qualititavely establishes reasonable accuracy for simulation of coplanar strip line at terahertz frequencies with open boundaries.

The difference between the simulated and theoretical propagation loss could be explained by two key assumptions of a time-domain simulation that are violated with the structure presented here. First, the surface impedance metal loss model is increasingly inaccurate as the metal strips become electrically thin. Second, at low

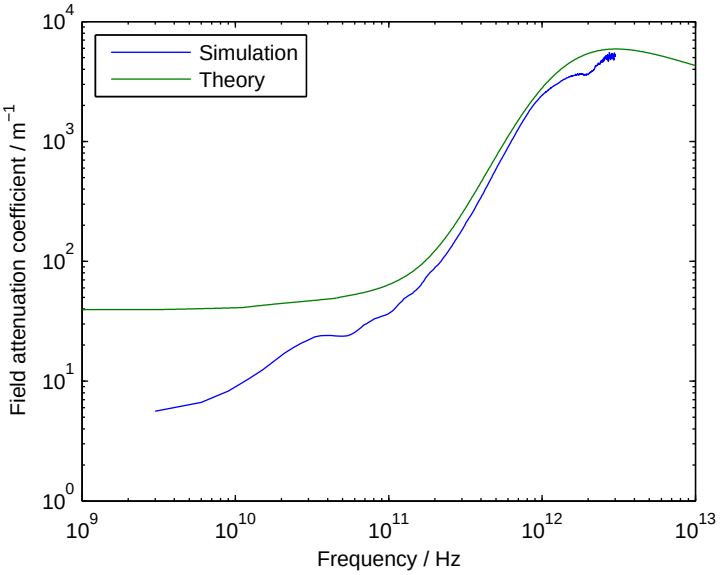

Figure 5.3: Comparison of the propagation loss of coplanar stripline obtained by simulation to theories of radiation and conduction loss.

frequencies the radiation boundary is not in the far field of the transmission line for the radiated wave. This is necessary to minimize computation requirements for the high frequencies.

Part III

Comparison and design of miniature devices

Chapter 6

Device candidates

Using the numerical techniques explored in Part II we will examine three devices in this Chapter for suitability as a miniature terahertz spectroscope. These three devices are reflection coupled antennas, angled transmission line, and covered transmission line. Analysis of these devices is presented in Sections 6.1, 6.2, and 6.3, respectively. These devices do not form a complete set of terahertz systems which could be used for spectroscopy, but they have been selected for practicality both in a simulation and real sense. If one is willing to consider exotic or somewhat impractical devices, there are many more types of devices which could be used for terahertz spectroscopy. For example, substrate integrated waveguide could be used with a slot in a waveguide wall to expose the field to a sample material.

6.1 Antennas without lenses

The common terahertz optical spectroscope fashioned with discrete components uses a pulsed laser stimulating photoconduction with the current driving an omnidirectional antenna fixed to a precisely machined dielectric (typically silicon) hemispherical lens [3, 4, 34]. In this Section, we will introduce a classification scheme for configu-

rations of coupled antennas and present qualitative observations of the simulated performance of reflection coupled antennas.

The first advantage with the use of directional antennas is miniaturization. The dielectric lenses typically employed in terahertz technology are several centimeters in diameter because they are constrained by geometric optics and the associated far field approximation requirements. Because many antenna designs depend on the operating wavelength, which is approximately 300 μm at 1 THz, an increase in antenna size to gain sufficient directivity is more than compensated for by the removal of a comparatively bulky centimeter-scale antenna. While the antennas for lens-antenna systems are already fabricated with planar lithography, removal of the lens may allow for improved alignment accuracy if more than one antenna is to be fabricated.

Further to the classification developed in Section 2.3.1, we can divide the configurations of antennas into four groups: broadside or end-fire, and dielectric half or full-space in the near field. While this scheme may be useful to classify antennas, we do not assert that any particular configuration of antenna is useful. Many broadside antenna designs require a dielectric half-space to be directive [13–15], whereas an end-fire antenna designed to operate in free space performs poorly when placed on a dielectric half-space [19]. An important consideration for broadside antennas is radiation direction. Many common designs, such as microstrip patch antennas, radiate most power in a direction perpendicular to the substrate. To efficiently couple two broadside antennas through reflection, the source antenna must radiate in the direction which reflects to the receiver antenna. This requirement complicates the design of reflection coupled broadside antennas. In contrast, end-fire antennas can easily be reflection coupled by rotating each antenna to make the proper angle for reflection without redesign of the antenna radiation pattern.

Additionally, some antennas may require an electrical matching network to im-

prove the bandwidth of usable power radiation. The implementation of this matching network may be difficult or impossible if it cannot be placed between the antenna feed point and terahertz source. The Yagi-Uda design has long been used for VHF radio reception. In this use, the antenna is mounted on a mast with any electrical matching networks being placed out of the plane of the antenna elements. For use in a terahertz photomixer, the Yagi-Uda design must be modified, usually by dividing the reflector in two parts to allow DC bias lines to connect to the driven dipole with a photoconductor at the center of the dipole [19]. Unfortunately, this design leaves no room for matching elements between the photoconductor and dipole. Matching elements are essential for broad source to far-field bandwidth in a Yagi-Uda design. Figure 6.1 schematically shows two representative Yagi-Uda antennas, and Figure 6.2 shows scattering parameters between two simulated Yagi-Uda antennas with a PEC reflector, illustrating the path loss and narrow bandwidth characteristics.

Alternative antenna designs, such as the log-periodic dipole array end-fire antenna, may accommodate a matching network between the source and antenna feed point but present other design problems. A log-periodic antenna designed for micrometer scale and decade bandwidth to cover 0.2 to 2.0 THz could have approximately 84 elements and be 8.5 mm in length according to a textbook design procedure [12]. Perhaps the most promising alternative antenna design is the TEM horn [20, 21]. The TEM horn borrows from the classic pyramidal horn but removes the side walls to separate the conductors for TEM propagation. Unfortunately this non-planar design is somewhat difficult to fabricate, requiring micro-manipulation of a metal plane.

Antennas are designed to operate in the far-field regime, so a terahertz spectroscope design would place the transmit and receive antennas in the far-field from each other and the target. However, possible applications of the terahertz spectroscope may require close proximity to a biological sample such as a live human in a clinic

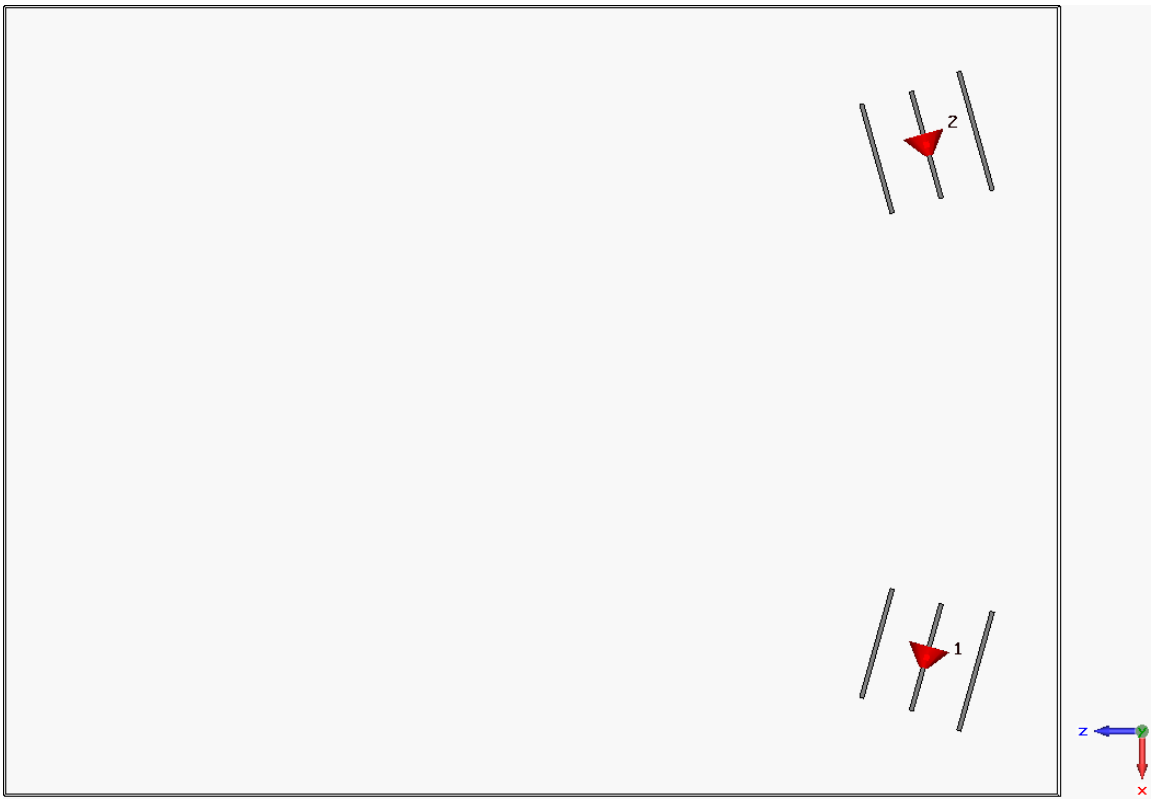

Figure 6.1: Two Yagi-Uda antennas with simulation bounds shown. The left-most boundary, in the z-direction, is an electric wall. The other five boundaries are perfectly matched layers. The red cones represent point-source ports where energy is introduced and absorbed.

environment or measuring an unknown sample in an industrial plant. These scenarios suggest impact and environmental protection is required. Such a protective membrane must be thin compared to the wavelength yet durable.

Coupled antennas are an interesting miniature method to perform terahertz spectroscopy but with common antenna designs are not suitable to replace the highly directive silicon lenses currently used in such systems. The main problem is lack of directivity due to antenna design or practical limitations.

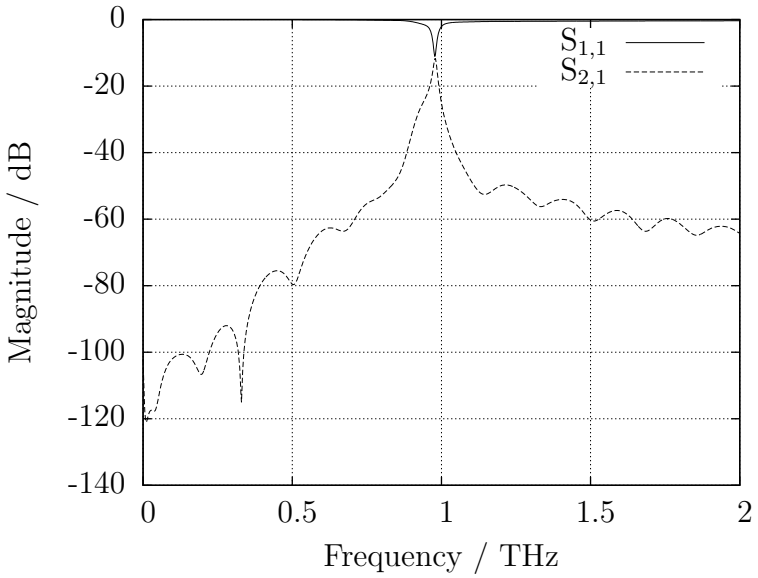

Figure 6.2: Scattering parameters between two Yagi-Uda antennas with a PEC reflector. The "AR- filter" function of CST Microwave Studio was used to extrapolate the time response for these narrow-band structures.

6.2 Angled transmission line

The reflection coupled antennas presented in Section 6.1 required significant physical separation of the antennas to allow far-field operation, as well as significant loss due to imperfect directivity. A natural solution to these problems, which has been previously proposed [92], is to simply remove the antennas and connect the terahertz generator and detector with a section of transmission line guiding a wave through reflection with the sample. We examined two configurations of coplanar stripline: where the strips lie in a plane perpendicular to the sample surface, and where the strips lie in planes perpendicular to a plane perpendicular to the sample surface.

Figure 6.3 shows a CAD model of the proposed device. By inspection, we see that the transmission line has a significant and uncompensated bend discontinuity where it meets the sample surface. Designing a transmission line compensator is difficult in this situation due to the unknown nature of the sample, which causes

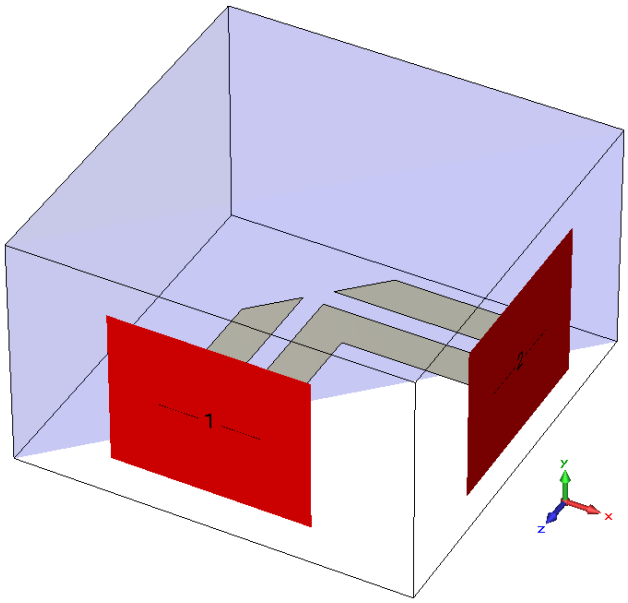

Figure 6.3: Perspective view of the CPS angle sensor.

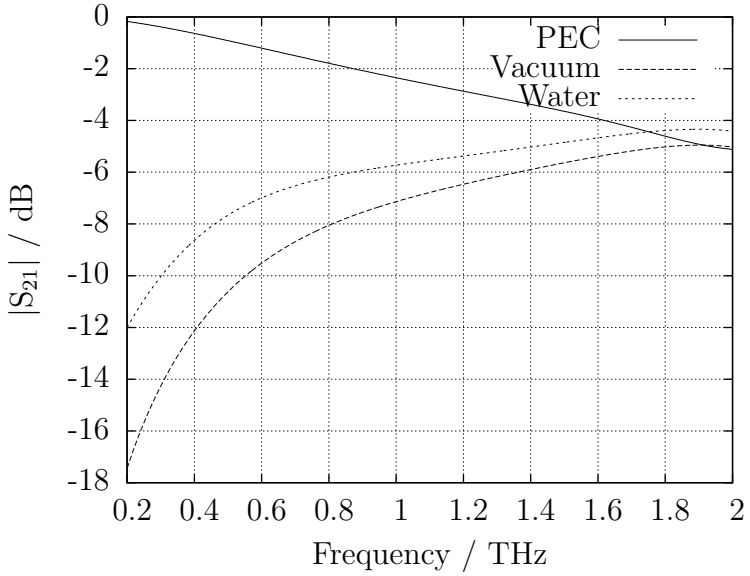

Figure 6.4: Transmission parameter of the CPS angle sensor.

reflection of unknown magnitude and phase. The device was simulated despite the high anticipated reflection to determine if it merits further investigation.

This device was simulated using CST Microwave Studio using the frequency domain solver with tetrahedral mesh, with a 45 degree angles of incidence and reflection, an air substrate to maximize reflection for testing purposes, and test samples of water (see Section 3.1.2), air, and PEC. The simulated device and its performance are shown in Figures 6.3 and 6.4, respectively. The water sample falls between the PEC and vacuum curves showing that PEC and vacuum define the limits. Therefore, the main problem with the angled transmission line sensor is a lack of dynamic range between the PEC and vacuum measurements.

The 45 degree configuration is easy to simulate because each of the transmission lines can be placed perpendicular to a boundary of the simulation. Some simulation software, such as CST Microwave Studio, uses the geometry of the waveguide port face to create an infinite extension of the transmission line, ideally resulting in zero reflection. Therefore, a wave on a transmission line not perpendicular to the simulation boundary would encounter a discontinuity at the simulation boundary. This reflection reduces the accuracy of the simulation.

6.3 Covered transmission line

The simple structure of a covered non-resonant transmission line has previously been proposed as a spectroscope, commonly in the form of a planar transmission line [28, 29, 93]. The simplicity of a planar transmission line device, where the sample is overlaid on the line on some substrate, belies its analytical complexity. A procedure to extract the unknown sample permittivity exists for coplanar waveguide, but that method assumes the fields are quasi-static [93]. In the present case, we desire a miniature

spectroscope operating at terahertz frequencies where the quasi-static assumption is not valid. Further analysis of this structure is presented in Chapter 7.

Chapter 7

Device comparison and design

In Chapter 6 we reviewed three possible devices for terahertz spectroscopy: antennas without lenses, angled transmission line, and covered transmission line. We compare these devices and select one for further evaluation as a balanced choice for broadband terahertz spectroscopy in Section 7.1. After selection, we present a simplified design procedure in Section 7.2.

7.1 Device comparison

The choice of a device for miniature terahertz spectroscopy is determined by the user's sensitivity to the variety of design trade-offs of such devices. Far field devices are typically easier to analyze but are subject to strong path loss and lack of space to implement matching circuits. Near field devices can deliver more power through the system but are very difficult to analyze.

Antennas without lenses are a natural first choice for a miniature device for terahertz spectroscopy. Assuming a highly directive antenna is used in place of a hyperhemispherical silicon lens, manufacturing is simplified and the complete device may be compactly fabricated. However, silicon lenses allow far more power than antennas

to be coupled into a beam directed at the target. This high directivity is necessary to overcome large path loss at terahertz frequencies, where path loss refers to the isotropic spreading loss in the Friis transmission equation.

Angled transmission line is a natural generalization of the coupled antennas concept, where the generated wave is guided through reflection from a sample material. However, the particular approach studied in Section 6.2 uses a notch in one of the two coplanar lines (illustrated in Figure 6.3) to allow the field concentrated in the center of the transmission line to interact more strongly with the sample. Unfortunately this design is not adequate due to low contrast between sample and no sample conditions especially at high frequencies, as shown in Figure 6.4.

A natural extension of the angled transmission line concept is to straighten the transmission line and allow the entire length of the line to interact with a sample material. This simplification allows more field to interact with the sample material and removes any reflections caused by an angle or similar features in the transmission line. However, the analysis of this type of line becomes very difficult over the broad terahertz frequency range due to the invalidity of the quasi-static field assumptions. Despite this limitation, covered transmission lines have advantages of sample to no sample contrast, physical size, and a relatively straightforward procedure to design the length or cover layer thickness. This procedure for covered transmission lines is presented in Section 7.2.

7.2 Design method

Our objective in this section is to develop a simple design procedure for a covered coplanar strip line sensor. This design will not include the photomixers or other structures intended to improve device performance. The design of a covered transmission

line sensor for strongly lossy sample materials depends on several variables: the desired power loss ratio between sample and no sample conditions, the transmission line length, and the difference between the propagation loss coefficients of the sample and no sample conditions, as follows:

$$-\frac{10\log_{10}\frac{P_2(d)}{P_1(d)}}{20\log_{10}e} = d(\alpha_2 - \alpha_1). \tag{7.1}$$

This equation is a restatement of Equation 5.3 to allow the user to easily substitute power ratios given in decibels. To design a transmission line sensor, the user must have sufficient specifications to determine missing variables. For example, minimum or maximum transmission line length, cover layer thickness, or allowable power loss with a highly lossy sample.

To begin the design process without an analytic solution for the propagation characteristics of coplanar stripline, we require a set of simulation results where some structural parameters of the transmission line are varied to obtain the desired propagation characteristics. For example, the coplanar stripline results presented in this Section were obtained from a stripline 10 μm in width, with 10 μm space between the conductors, and with 1 μm thick metal strips. Results from much thinner strips have been published [23], but the particular value of 1 μm was arbitrarily chosen here to decrease the frequency where the skin depth equals one fifth the strip thickness to 0.14 THz, to allow the use of the surface impedance model (as reviewed in Section 4.1) for metal loss.

The parameters of strip width, spacing, and thickness each affect the conduction loss, radiation loss and dielectric loss (through modifying the field distribution) of the transmission line. For a single frequency and only considering conduction and radiation losses, there exists one frequency for given strip dimensions which minimizes

the sum of those losses. Because this minimum exists only for one frequency, the strip parameters for simulation were chosen as round numbers (10 μm) close to the minimum for 1 THz.

We present two sets of simulation results in Figures 7.1 and 7.2. These curves represent the difference between field loss coefficients for waves propagating on coplanar stripline with a silica substrate and silica superstrate or BCB superstrate, respectively. The sample material in both cases is water, with the dispersion and loss of these materials as presented in Chapter 3.

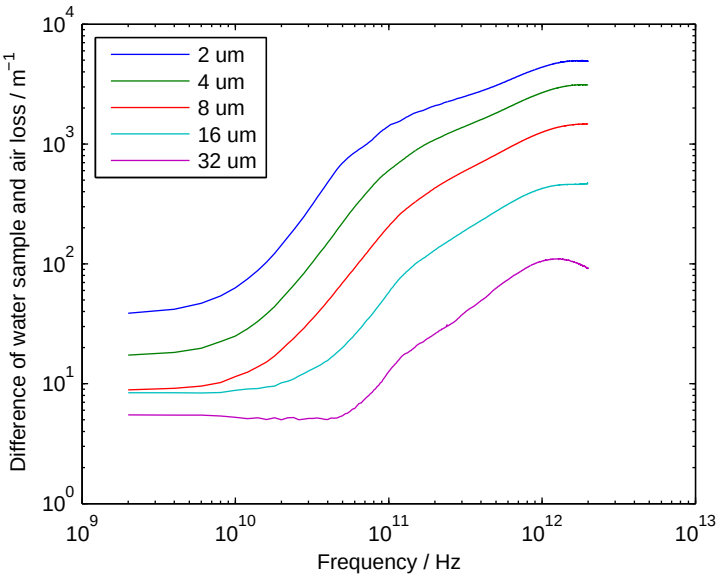

Figure 7.1: Difference between loss coefficients while varying superstrate thickness, for a CPS with silica substrate and superstrate

To illustrate the use of the design procedure, we will work through a simple example where only the cover layer thickness is the unknown variable. Assume that we desire a 20 dB difference in power loss ($10log_{10}P_2(d)/P_1(d) = 20$) with and without a sample between the source and detector at a frequency of 1 THz. Additionally, we desire a device approximately 1 cm long. According to equation 7.1 we must design a device with loss difference (the term $\alpha_2 - \alpha_1$) of approximately 230.3. Assuming

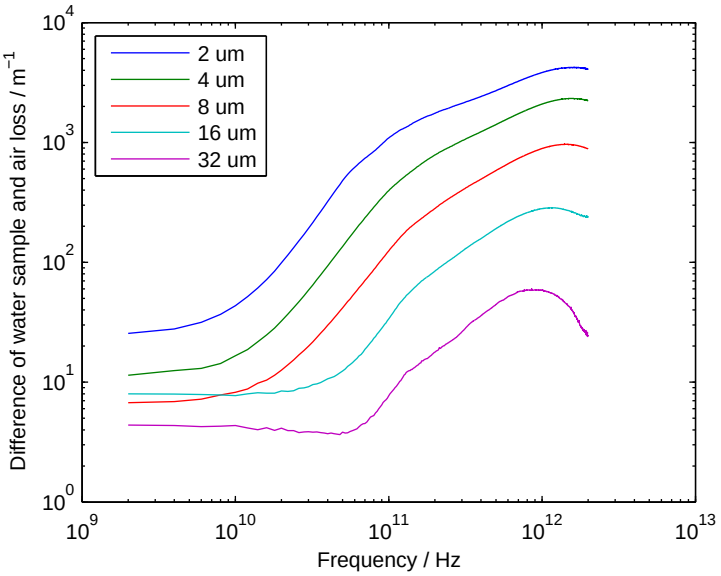

Figure 7.2: Difference between loss coefficients while varying superstrate thickness, for a CPS with silica substrate and BCB superstrate

we wish to use a sililca substrate and superstrate, we refer to Figure 7.1 to obtain an estimate of the cover layer thickness to satisfy our requirements. Additionally, under the hypothesis that the loss difference follows a double-exponential law according to the cover layer thickness, we may perform a nonlinear least squares curve fit with the data from Figure 7.1 at 1 THz to obtain an estimate for the appropriate cover layer thickness. The double exponential model used is:

$$\alpha_\Delta(t) = Ae^{Bt} + Ce^{Dt}. \tag{7.2}$$

Using the root-finding function `fzero` in MATLAB we calculate the required cover layer thickness for a silica-silica system as 22.3 μm. A cross-sectional view of the designed device is shown in Figure 7.3.

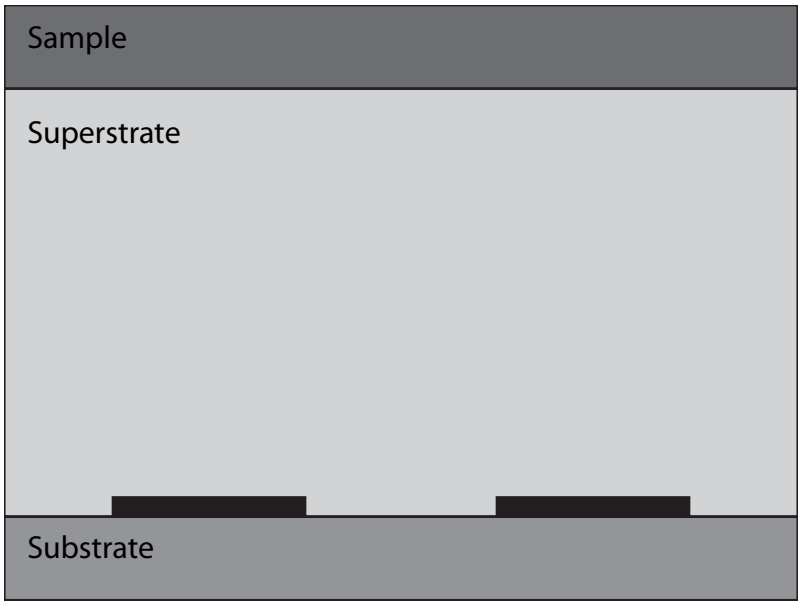

Figure 7.3: A cross-sectional view of a coplanar stripline with designed loss characteristic

Part IV

Conclusions and contributions

Chapter 8

Conclusions

Despite its relative youth, a diverse array of technologies has been created to perform science with terahertz waves. It is obvious that every technology has advantages and limitations relative to its alternatives, but at terahertz frequencies the advantages and limitations often do not show a clear choice for a particular application. Many methods of terahertz generation are not very powerful and so the large dielectric lenses used for a terahertz spectroscopy apparatus are virtually required unless the user is willing to sacrifice received signal power.

While far field devices struggle with directing power to their targets, near field devices struggle with complexity of analysis. While inversion of the propagation calculation is possible for low frequencies, where material dispersion can be simplified, no such simplification is possible at terahertz frequencies. Without analytical formulas for the propagation characteristics of planar transmission lines, one must resort to techniques such as interpolating results from numerical simulations.

Simulating terahertz structures, especially in broad-band time-domain numerical codes, can be complex with significant potential for error. One must be aware of the capabilities and limitations of a particular code, such as the behaviour of disper-

sive materials adjacent to radiation boundaries, which can cause instability in some codes. Additionally, realistic models of materials may not be valid at all simulated frequencies.

Realistic material models are required for broad-band characterization of terahertz devices. Many common materials used in terahertz systems, such as gallium arsenide and silica glass, are dispersive over the broad bandwidth commonly used for terahertz applications. In addition to material dispersion, common transmission line structures can have strong waveguide dispersion at terahertz frequencies. The combination of material dispersion and waveguide dispersion is well known in optical fiber technologies, but unfortunately one cannot simply insert a length of dispersion-compensating fiber into a terahertz spectroscope. Models and understanding of dispersion are essential to design of terahertz systems.

However, the particular covered coplanar strip transmission line studied showed high contrast between lossy and non-lossy samples with a simple configuration and most importantly no terahertz optics. If one can extract the permittivity of an unknown sample from simulation results, this structure would allow a truly miniature terahertz spectroscope (disregarding the size of the lasers or other source of excitation). The challenge remains to analytically explain the characteristics of covered transmission lines over a broad bandwidth and to confirm that theory by building and testing such a device in a rigorous fashion.

Chapter 9

Contributions

In Chapters 3 and 4 we reviewed and provided typical parameters for broadband far-infrared models for the permittivity of non-metallic and metallic materials, respectively. The model parameters presented in those Chapters were derived from least squares fitting of experimental data provided by others. Because loss and dispersion in materials generally cannot be ignored at terahertz frequencies, these models can be used to provide realistic results from numerical simulation tools.

In Chapter 6, we presented simulation results of three miniature devices for terahertz spectroscopy. Confidence in these simulation results was greatly enhanced through the previously discussed material models. These simulation results showed that typical antenna designs struggle to overcome the large path loss at terahertz frequencies even over path lengths of just several hundred micrometers. In addition to path loss, the simulated antennas did not leave room for a matching or bias network in their planar structure, leaving physical realization an open problem.

The covered coplanar stripline discussed in Section 6.3 showed promise for miniature terahertz applications, with some difficulties in simulation. We developed simulation techniques for broadband time-domain numerical codes to overcome problems

with measuring power of the propagating wave and ensuring radiation loss from the asymmetric structure (in the transverse sense) was accurately removed from the computation domain.

With these simulation results, we presented a simple procedure to design the loss per length of covered coplanar stripline in Section 7.2. This method allows the user to design the length or other parameters of the device given some information on the difference between the propagation loss with and without some desired lossy sample material present.

References

[1] B. Schulkin. *Miniature Time-Domain Terahertz Spectroscopy*. PhD thesis, Rensselaer Polytechnic Institute, Troy, New York, December 2008.

[2] B. Schulkin, B. Clough, D. Brigada, N. Laman, T. Tongue, and X.-C. Zhang. Progress toward handheld THz spectrometry. In *34th International Conference on Infrared, Millimeter, and Terahertz Waves*, Busan, Korea, September 2009. IEEE.

[3] C. A. Schmuttenmaer. Exploring dynamics in the far-infrared with terahertz spectroscopy. *Chemical Reviews*, 104(4):1759–1780, 2004.

[4] P. H. Siegel. Terahertz technology. *IEEE Transactions on Microwave Theory and Techniques*, 50(3):910–928, March 2002.

[5] M. C. Beard, G. M. Turner, and C. A. Schmuttenmaer. Terahertz spectroscopy. *Journal of Physical Chemistry B*, 106(29):7146–7159, 2002.

[6] J. Horvat and R. A. Lewis. Peeling adhesive tape emits electromagnetic radiation at terahertz frequencies. *Optics Letters*, 34(14):2195–2197, July 2009.

[7] B. W. J. McNeil and N. R. Thompson. X-ray free-electron lasers. *Nature Photonics*, 4(12):814–821, December 2010.

[8] D. Saeedkia and S. Safavi-Naeini. Terahertz photonics: Optoelectronic techniques for generation and detection of terahertz waves. *Journal of Lightwave Technology*, 26(15):2409–2423, August 2008.

[9] M. J. E. Golay. Theoretical consideration in heat and infra-red detection, with particular reference to the pneumatic detector. *The Review of Scientific Instruments*, 18(5):347–356, May 1947.

[10] M. J. E. Golay. A pneumatic infra-red detector. *The Review of Scientific Instruments*, 18(5):357–362, May 1947.

[11] T. J. Parker, J. E. Ford, W. G. Chambers, and C. L. Mok. A Fourier spectrometer for determining the optical constants of transparent solids in the far-infrared from 77 to 300 K. *Infrared Physics*, 18(5–6):571–576, December 1978.

[12] C. A. Balanis. *Antenna Theory: Analysis and Design.* John Wiley & Sons, Inc., Hoboken, New Jersey, third edition, 2005.

[13] N. K. Das. Dielectric-lens coupled printed dipole for millimeter wave applications: analysis using a hybrid spectral-domain mehtod. In *Antennas and Propagation Society International Symposium*, pages 1902–1905, July 1992.

[14] R. C. Compton, R. C. McPhedran, Z. Popović, G. M. Rebeiz, P. P. Tong, and D. B. Rutledge. Bow-tie antennas on a dielectric half-space: theory and experiment. *IEEE Transactions on Antennas and Propagation*, 35(6):622–631, June 1987.

[15] M. Kominami, D. M. Pozar, and D. H. Schaubert. Dipole and slot elements and arrays on semi-infinite substrates. *IEEE Transactions on Antennas and Propagation*, 33(6):600–607, June 1985.

[16] E. R. Brown, A. W. M. Lee, B. S. Navi, and J. E. Bjarnason. Characterization of a planar self-complimentary square-spiral antenna in the THz region. *Microwave and Optical Technology Letters*, 48(3):524–529, March 2006.

[17] D. R. Jackson and N. G. Alexópoulos. Gain enhancement methods for printed circuit antennas. *IEEE Transactions on Antennas and Propagation*, 33(9):976–987, September 1985.

[18] G. Lovat, P. Burghignoli, F. Capolino, and D. R. Jackson. Combinations of low/high permittivity and/or permeability substrates for highly directive planar metamaterial antennas. *IET Microwaves, Antennas & Propagation*, 1(1):177–183, February 2007.

[19] C. Sydlo, J. Sigmund, H. L. Hartnagel, R. Mendis, M. Feiginov, and P. Meissner. Planar terahertz antenna optimisation. In *IEEE/ACES International Conference on Wireless Communications and Applied Computational Electromagnetics*, pages 878–882, April 2005.

[20] E. Peytavit, J.-F. Lampin, T. Akalin, and L. Desplanque. Integrated terahertz TEM horn antenna. *Electronics Letters*, 43(2):73–75, January 2007.

[21] T. Akalin, J.-F. Lampin, E. Peytavit, S. Barbieri, W. Maineult, C. Sirtori, J. Alton, H. E. Beere, and D. A. Ritchie. QCL with terahertz TEM-horn antennas. In *Joint 32nd International Conference on Infrared and Millimeter Waves and 15th Internation Conference on Terahertz Electronics*, pages 474–475, September 2007.

[22] D. Grischkowsky, I. N. Duling, III, J. C. Chen, and C.-C. Chi. Electromagnetic shock waves from transmission lines. *Physical Review Letters*, 59(15):1663–1666, October 1987.

[23] M. Y. Frankel, S. Gupta, J. A. Valdmanis, and G. A. Mourou. Terahertz attenuation and dispersion charactersistics of coplanar transmission lines. *IEEE Transactions on Microwave Theory and Techniques*, 39(6):910–916, June 1991.

[24] L. Desplanque, E. Peytavit, J.-F. Lampin, D. Lippens, and F. Mollot. Shock wave coupling between terahertz transmission lines on GaAs. *Applied Physics Letters*, 83(12):2483–2485, September 2003.

[25] H.-J. Cheng, J. F. Whitaker, T. M. Weller, and L. P. B. Katehi. Terahertz-bandwidht characteristics of coplanar transmission lines on low permittivity substrates. *IEEE Transactions on Microwave Theory and Techniques*, 42(12):2399–2406, December 1994.

[26] D. Saeedkia and S. Naeini-Safavi. Modeling and analysis of a multilayer dielectric slab waveguide with applications in edge-coupled terahertz photomixer sources. *Journal of Lightwave Technology*, 25(1):432–439, January 2007.

[27] R. W. McGowan, D. Grischkowsky, and J. A. Misewich. Demonstrated low radiative loss of a quadrupole ultrashort electrical pulse propagated on a three strip coplanar transmission line. *Applied Physics Letters*, 71(19):2842–2844, November 1997.

[28] T. Ohkubo, M. Onuma, J. Kitagawa, and Y. Kadoya. Micro-strip-line-based sensing chips for characterization of polar liquids in terahertz regime. *Applied Physics Letters*, 88(21):212511, 2006.

[29] Y. Kadoya, M. Onuma, S. Yanagi, T. Ohkubo, N. Sato, and J. Kitagawa. THz wave propagation on strip lines: devices, properties, and applications. *Radioengineering*, 17(2):48–55, June 2008.

[30] M. Nagel, F. Richter, P. Haring Bolívar, and H. Kurz. A functionalized THz sensor for marker-free DNA analysis. *Physics in Medicine and Biology*, 48(22):3625–3636, 2003.

[31] J. Zhang. *A cylindrical dielectric whispering-gallery mode terahertz cavity coupled with a dielectric slab waveguide*. PhD thesis, Oklahoma State University, August 2002.

[32] M. Neshat, D. Saeedkia, R. Sabry, and S. Safavi-Naeini. An integrated continuous-wave terahertz biosensor. In J. O. Jensen and H.-L. Cui, editors, *Terahertz for Military and Security Applications V*, volume 6549. SPIE, 2007.

[33] M. Raum. Quasioptical measurement of ferrite material parameters at terahertz frequencies by a new method: Faraday angle resonance. *International Journal of Infrared and Millimeter Waves*, 13(7):1211–1227, 1994.

[34] R. M. Woodward, B. E. Cole, V. P. Wallace, R. J. Pye, D. D. Arnone, E. H. Linfield, and M. Pepper. Terahertz pulse imaging in reflection geometry of human skin cancer and skin tissue. *Physics in Medicine and Biology*, 47(21):3853–3863, 2002.

[35] R. M. Woodward, V. P. Wallace, R. J. Pye, B. E. Cole, D. D. Arnone, E. H. Linfield, and M. Pepper. Terahertz pulse imaging of ex vivo basal cell carcinoma. *Journal of Investigative Dermatology*, 120(1):72–78, 2003.

[36] V. P. Wallace, A. J. Fitzgerald, S. Shankar, N. Flanagan, R. Pye, J. Cluff, and D. D. Arnone. Terahertz pulsed imaging of basal cell carcinoma ex vivo and in vivo. *British Journal of Dermatology*, 151(2):424–432, 2004.

[37] E. Pickwell, B. E. Cole, A. J. Fitzgerald, M. Pepper, and V. P. Wallace. In vivo study of human skin using pulsed terahertz radiation. *Physics in Medicine and Biology*, 49(9):1595–1608, 2004.

[38] H. R. Philipp. Silicon dioxide (SiO_2) (glass). In E. D. Palik, editor, *Handbook of Optical Constants of Solids*, volume 1, pages 749–763. Academic Press, Inc., San Diego, CA, 1985.

[39] R. Kitamura, L. Pilon, and M. Jonasz. Optical constants of silica glass from extreme ultraviolet to far infrared at near room temperature. *Applied Optics*, 46(33):8118–8133, November 2007.

[40] E. Schlömann. Dielectric losses in ionic crystals with disordered charge distributions. *Physical Review*, 135(2A):A413–A419, July 1964.

[41] U. Strom and P. C. Taylor. Temperature and frequency dependences of the far-infrared and microwave optical absorption in amorphous materials. *Physical Review B*, 16(12):5512–5522, December 1977.

[42] M. Naftaly and R. E. Miles. Terahertz time-domain spectroscopy of silicate glasses and the relationship to material properties. *Journal of Applied Physics*, 102(4):043517, 2007.

[43] D. W. Berreman and F. C. Unterwald. Adjusting poles and zeros of dielectric dispersion to fit reststrahlen of $PrCl_3$ and $LaCl_3$. *Physical Review*, 174(3):791–799, October 1968.

[44] H. Selig, M. Khazan, and I. Wilke. Optical properties of glasses and ceramics for terahertz-technology. In *Conference on Lasers and Electro-Optics Europe*, page CTuK113, Nice, France, September 2000.

[45] S. Kojima, H. Kitahara, S. Nishizawa, Y. S. Yang, and M. W. Takeda. Terahertz time-domain spectroscopy of low-energy excitations in glasses. *Journal of Molecular Structure*, 744–747:243–246, June 2005.

[46] T. Ohsaka and S. Oshikawa. Effect of OH content on the far-infrared absorption and low-energy states in silica glass. *Physical Review B*, 57(9):4995–4998, March 1998.

[47] L. Ghivelder and W. A. Phillips. Far infrared absorption in disordered solids. *Journal of Non-Crystalline Solids*, 109(2–3):280–288, June 1989.

[48] K. W. Hutt, W. A. Phillips, and R. J. Butcher. Far-infrared properties of dilute hydroxyl groups in an amorphous silica matrix. *Journal of Physics: Condensed Matter*, 1(29):4767–4772, July 1989.

[49] C. M. Randall and R. D. Rawcliffe. Refractive indices of germanium, silicon, and fused quartz in the far infrared. *Applied Optics*, 6(11):1889–1895, November 1967.

[50] D. C. Dube, M. T. Lanagan, J. H. Kim, and S. J. Jang. Dielectric measurements on substrate materials at microwave frequencies using a cavity perturbation technique. *Journal of Applied Physics*, 63(7):2466–2468, April 1988.

[51] T. Henning and H. Mutschke. Low-temperature infrared properties of cosmic dust analogues. *Astronomy and Astrophysics*, 327(2):743–754, November 1997.

[52] T. J. Parker, J. E. Ford, and W. G. Chambers. The optical constants of pure fused quartz in the far-infrared. *Infrared Physics*, 18(3):215–219, May 1978.

[53] C. Koike, H. Hasegawa, N. Asada, and T. Komatuzaki. Optical constants of fine particles for the infrared region. *Monthly Notices of the Royal Astronomical Society*, 239:127–137, 1989.

[54] R. K. Bogens and A. G. Zhukov. The optical constants of fused quartz in the far infrared. *Journal of Applied Spectroscopy*, 4(1):54–55, 1966.

[55] A. P. Zhilinskii, A. P. Gorchakov, T. S. Egorova, and N. A. Miskinova. Optical characteristics of fused quartz in the far IR range. *Optics and Spectroscopy*, 62(6):783–784, June 1987.

[56] M. Miler. Infrared absorption of glassy silicon dioxide. *Czechoslovak Journal Of Physics*, 18(3):354–362, 1968.

[57] S. Popova, T. Tolstykh, and V. Vorobev. Optical characteristics of amorphous quartz in the 1400-200 cm^{-1} region. *Optical Spectroscopy*, 33:444–445, 1972.

[58] A. M. Efimov and V. G. Pogareva. IR absorption spectra of vitreous silica and silicate glasses: The nature of bands in the 1300 to 5000 cm^{-1} region. *Chemical Geology*, 229(1–3):198–217, May 2006.

[59] W. Bagdade and R. Stolen. Far infrared absorption in fused quartz and soft glass. *Journal of Physics and Chemistry of Solids*, 29(11):2001–2008, November 1968. Incorrectly cited as "Bagdad" in Google Scholar.

[60] H. R. Philipp. The infrared optical properties of sio_2 and sio_2 layers on silicon. *Journal of Applied Physics*, 50(2):1053–1057, February 1979.

[61] C. Andeen, D. Schuele, and J. Fontanella. Effect of OH^- on the low-frequency dielectric constant of vitreous silica. *Journal of Applied Physics*, 45(4):1071–1074, March 1974.

[62] P. J. W. Debye. *Polar Molecules*. The Chemical Catalog Company, New York, 1929.

[63] C. Rønne, L. Thrane, P.-O. Åstrand, A. Wallqvist, K. V. Mikkelsen, and S. R. Keiding. Investigation of the temperature dependence of dielectric relaxation in liquid water by THz reflection spectroscopy and molecular dynamics simulation. *Journal of Chemical Physics*, 107(14):5319–5331, 1997.

[64] E. Perret, N. Zerounian, S. David, and F. Aniel. Complex permittivity characterization of benzocyclobutene for terahertz applications. *Microelectronic Engineering*, 85(11):2276–2281, 2008.

[65] C. J. Johnson, G. H. Sherman, and R. Weil. Far infrared measurement of the dielectric properties of GaAs and CdTe at 300 K and 8 K. *Applied Optics*, 8(8):1667–1671, August 1969. The captions of Figures 2 and 3 are swapped with Figures 4 and 5, respectively.

[66] P. G. Huggard, J. A. Cluff, G. P. Moore, C. J. Shaw, S. R. Andrews, S. R. Keiding, E. H. Linfield, and D. A. Ritchie. Drude conductivity of highly doped GaAs at terahertz frequencies. *Journal of Applied Physics*, 87(5):2382–2385, March 2000.

[67] T. Skauli, P. S. Kuo, K. L. Vodopyanov, T. J. Pinguet, O. Levi, L. A. Eyres, J. S. Harris, M. M. Fejer, B. Gerard, L. Becouarn, and E. Lallier. Improved dispersion relations for GaAs and applications to nonlinear optics. *Journal of Applied Physics*, 94(10):6447–6455, November 2003.

[68] D. Grischkowsky, S. Keiding, M. van Exter, and C. Fattinger. Far-infrared time-domain spectroscopy with terahertz beams of dielectrics and semiconductors. *Journal of the Optical Society of America B*, 7(10):2006–2015, October 1990.

[69] D. F. Parsons and P. D. Coleman. Far infrared optical constants of gallium phosphide. *Applied Optics*, 10(7):1683–1685, July 1971.

[70] A. Borghesi and G. Guizzetti. Gallium phosphide (GaP). In E. D. Palik, editor, *Handbook of Optical Constants of Solids*, volume 1, pages 445–464. Academic Press, Inc., San Diego, CA, 1985.

[71] D. M. Pozar. *Microwave Engineering*. John Wiley & Sons, Inc., New York, second edition, 1998.

[72] P. Drude. Zur Elektronentheorie der Metalle. *Annalen der Physik*, 306(3):566–613, 1900.

[73] P. Drude. Zur Elektronentheorie der Metalle; Galvanomagnetische und thermomagnetische Effecte. *Annalen der Physik*, 308(11):369–402, 1900.

[74] M. A. Ordal, L. L. Long, R. J. Bell, S. E. Bell, R. R. Bell, R. W. Alexander, Jr., and C. A. Ward. Optical properties of the metals Al, Co, Cu, Au, Fe, Pb, Ni, Pd, Pt, Ag, Ti, and W in the infrared and far infrared. *Applied Optics*, 22(7):1099–1120, April 1983.

[75] N. Katzenellenbogen and D. Grischkowsky. Electrical characterization to 4 THz of N- and P-type GaAs using THz time-domain spectroscopy. *Applied Physics Letters*, 61(7):840–842, August 1992.

[76] R. J. Sheppard, B. P. Jordan, and E. H. Grant. Least squares analysis of complex data with applications to permittivity measurements. *Journal of Physics D: Applied Physics*, 3(11):1759–1764, 1970.

[77] R. J. Sheppard. The least-squares analysis of complex weighted data with dielectric applications. *Journal of Physics D: Applied Physics*, 6(6):790–794, 1973.

[78] P. B. Johnson and R. W. Christy. Optical constants of the noble metals. *Physical Review B*, 6(12):4370–4379, December 1972.

[79] L. G. Schulz and F. R. Tangherlini. Optical constants of silver, gold, copper, and aluminum. II. The index of refraction n. *Journal of the Optical Society of America*, 44(5):362–368, May 1954.

[80] L. G. Schulz and F. R. Tangherlini. Optical constants of silver, gold, copper, and aluminum. I. The absorption coefficient k. *Journal of the Optical Society of America*, 44(5):357–362, May 1954.

[81] G. Brändli and A. J. Sievers. Absolute measurement of the far-infrared surface resistance of Pb. *Physical Review B*, 5(9):3550–3557, May 1972.

[82] V. G. Padalka and I. N. Shklyarevskii. Determination of the microcharacteristics of silver and gold from the infrared optical constants and the conductivity at 82 and 295 K. *Optics and Spectroscopy*, 11:285, October 1961.

[83] G. P. Motulevich and A. A. Shubin. Influence of Fermi surface shape in gold on the optical constants and Hall effect. *Soviet Physics JETP*, 20:560, October 1965.

[84] G. A. Bolotin, A. N. Voloshinksii, M. M. Kirillova, M. M. Neskov, A. V. Sokolov, and B. A. Charikov. Optical properties of titanium and vanadium in the infrared range of the spectrum. *The Physics of Metals and Metallography*, 13:823, 1962.

[85] H. E. Bennett and J. M. Bennett. Validity of the Drude theory for silver, gold and aluminum in the infrared. In F. Abelès, editor, *Optical properties and electronic structure of metals and alloys*, page 175. North-Holland Pub. Co., Amsterdam, 1966.

[86] J. H. Weaver, C. Krafka, D. W. Lynch, and E. E. Koch. *Optical Properties of Metals II: Noble Metals, Aluminum, Lanthanides, and Actinides,* $0.1 \leq h\nu \leq 500$

eV. Fachinformationszentrum Energie, Physik, Mathematik GmbH, Karlsruhe, Germany, 1981.

[87] P. G. Etchegoin, E. C. Le Ru, and M. Meyer. An analytic model for the optical properties of gold. *The Journal of Chemical Physics*, 125(16):164705, 2006.

[88] R. A. Matula. Electrical resistivity of copper, gold, palladium, and silver. *Journal of Physical and Chemical Reference Data*, 8(4):1147–1298, October 1979.

[89] G. Pass and H. Sutcliffe. Measurement of magnetic susceptibilities and the adoption of SI units. *Journal of Chemical Education*, 48(3):180–181, March 1971.

[90] M. Garber, W. G. Henry, and H. G. Hoeve. A magnetic susceptibility balance and the temperature dependence of the magnetic susceptibility of copper, silver, and gold, 295–975 K. *Canadian Journal of Physics*, 38(12):1595–1613, 1960.

[91] C. L. Holloway. Expressions for the conductor loss of strip-line and coplanar-strip (CPS) structures. *Microwave and Optical Technology Letters*, 25(3):162–168, May 2000.

[92] F. Afshinmanesh and T. E. Darcie. Terahertz radiation in biology: study on analytical model of skin, investigation on non-invasive detection of blood-glucose, design of terahertz sensors. Unpublished, Department of ECE, University of Victoria, March 2008.

[93] A. Raj, W. S. Holmes, and S. R. Judah. Wide bandwidth measurement of complex permittivity of liquids using coplanar lines. *IEEE Transactions on Instrumentation and Measurement*, 50(4):905–909, August 2001.